Insights into the dynamics of mafic magmatic-hydromagmatic eruptions from volatile degassing behaviour: The Hverfjall Fires, Iceland

E.J. Liu[*1], K.V. Cashman[2], A.C. Rust[2] & M. Edmonds[1]

[1]Department of Earth Sciences, University of Cambridge, Downing Street, Cambridge, CB2 3EQ, UK.

[2]School of Earth Sciences, University of Bristol, Wills Memorial Building, Bristol, BS81RJ, UK.

*Corresponding author: EJL (ejl54@cam.ac.uk)

Abstract

The style and intensity of hydromagmatic activity is governed by a complex interplay between the relative volumes of magma and water that interact, their relative viscosities, the depth of subsurface explosions, the substrate properties, and the vent geometry. Fundamental questions remain, however, regarding the role of magmatic vesiculation in determining the dynamics of magma-water interaction (MWI). Petrological reconstructions of magmatic degassing histories are commonly employed to interpret the pre- and syn-eruptive conditions during 'dry' magmatic eruptions, but the application of similar techniques to hydromagmatic activity has not yet been fully explored. In this study, we integrate glass volatile measurements (S, Cl, H_2O and CO_2) with field observations and microtextural measurements to examine the relationship between degassing and eruptive style during the Hverfjall Fires fissure eruption, Iceland. Here, coeval fissure vents produced both 'dry' magmatic (Jarðbaðshólar scoria cone complex) and variably wet hydromagmatic (Hverfjall tuff ring) activity, generating physically distinct pyroclastic deposits with contrasting volatile signatures. Matrix glass volatile concentrations in hydromagmatic ash (883 ± 172 [1σ] ppm S; 0.45 ± 0.03 [1σ] wt% H_2O; ≤20 ppm CO_2) are consistently elevated relative to magmatic ash and scoria lapilli (418 ± 93 [1σ] ppm S; 0.12 ± 0.48 [1σ] wt% H_2O; CO_2 below detection) and overlap with the range for co-erupted

phenocryst-hosted melt inclusions (1522 ± 127 [1σ] ppm S; 165 ± 27 [1σ] ppm Cl). Measurements of hydromagmatic glasses indicate that the magma has degassed between 17 and 70% of its initial sulfur prior to premature quenching at variably elevated confining pressures.

By comparing volatile saturation pressures for both magmatic and hydromagmatic glasses, and how these vary through the eruptive stratigraphy, we place constraints on the conditions of MWI. Crucially, our data demonstrate that the magma was already vesiculating when it encountered groundwater at depths of 100–200 m, and that the external water supply was sufficient to maintain MWI throughout the eruption with no significant vertical or lateral migration of the fragmentation surface. We propose that development of an in-vent water-sediment slurry provides a mechanism through which the elevated confining pressures of ~1.6–2.6 MPa (or up to 6 MPa accounting for uncertainty in CO_2 below analytical detection) could be maintained and buffered throughout the eruption, whilst enabling vertical mixing and ejection of fragmented juvenile and lithic material from a range of depths. Importantly, these results demonstrate that the volatile contents of hydromagmatic deposits provide valuable records of (1) the environment of MWI (e.g., groundwater versus surface water, vertical migration of the fragmentation level) and (2) the state of the magma at the time of fragmentation and quenching. We further suggest that the volatile content of tephra glasses provides a reliable alternative (or additional) indicator of a hydromagmatic origin, particularly for reduced Ocean Island Basalts where late-stage volatile saturation and degassing (S, H_2O) occurs over a pressure range relevant to typical MWI environments.

Keywords

hydromagmatism, Hverfjall Fires, Iceland, volatiles

1. Introduction

Hydromagmatic eruptions are generated by the explosive interaction of magma with external water. In contrast to 'dry' basaltic eruptions that are driven purely by the rapid exsolution and expansion of magmatic volatiles (Mangan and Cashman, 1996; Parfitt, 1998; Mangan et al., 2014), the energy released during magma-water interaction (MWI) is further influenced by the efficiency of heat exchange with water and/or steam. Energetic water vaporisation/expansion during MWI causes extensive melt fragmentation, which is enhanced by the brittle response of silicate melt to rapid quenching (e.g., Lorenz, 1975; Peckover et al., 1973; Colgate and Sigurgeirsson, 1973; Sheridan and Wohletz, 1983; Kokelaar, 1986; Wohletz, 1986; Zimanowski et al., 1991, 1997; Büttner et al., 2002; Van Otterloo et al., 2015; Cashman and Scheu, 2015; Liu et al., 2015, 2017). High vesicularities and bubble number densities within some hydromagmatic pyroclasts demonstrate that significant vesiculation can take place prior to MWI (Mastin et al., 2004; Murtagh et al., 2011; Rausch et al., 2015; Liu et al., 2015, 2017), with the shape and size distributions of fragmented particles determined by the bubble population at the time of quenching and brittle fragmentation. Magma ascent histories and degassing budgets can be reconstructed from the volatile concentrations preserved within pristine melt inclusions and the matrix glass of erupted pyroclasts (e.g., Þórðarson et al., 1996; Metrich et al., 1991, 2010; Þórðarson and Self, 2003; Wallace 2003; Edmonds, 2008; Metrich and Wallace, 2008; Self et al., 2008; Johnson et al., 2010; Wallace and Edmonds, 2011; Hartley et al., 2014; Wallace et al., 2015). Yet, similar geochemical approaches to explore the dynamics of MWI remain comparatively under-utilised.

Mixed eruptions including both magmatic and hydromagmatic phases (either at a single vent or at different vents along an active fissure) are common in Iceland due to the abundance of external water sources within volcanic environments. Icelandic tephra erupted during hydromagmatic and magmatic activity have distinct residual volatile compositions, with matrix

glass sulfur concentrations (S_{MG}) consistently elevated within hydromagmatic pyroclasts (Þórðarson et al., 1996, 2001, 2003; Óladóttir et al., 2008; Sigmarsson et al., 2013; Schipper et al., 2015). The Laki fissure eruption of 1783–84 provides an illustrative example of a mixed eruption: hydromagmatic tephra comprises ~20% of the total tephra volume, with the remainder produced by 'dry' Strombolian activity. Laki hydromagmatic glasses contain variable but elevated S_{MG} (490–1260 ppm; average 933 ± 212 ppm), whilst Strombolian glasses contain uniformly low S_{MG} concentrations (418–640 ppm; average 490 ± 82 ppm; Þórðarson et al., 1996). These residual sulfur concentrations correspond to contrasting degassing efficiencies of 25–70% and 62–75% for hydromagmatic and magmatic activity, respectively, relative to the initial sulfur content of 1677 ± 225 ppm preserved in olivine-hosted melt inclusions (S_{MI}; Metrich et al., 1991; Þórðarson et al., 1996).

The progressive exsolution of sulfur with decreasing magma overpressure is well-recorded in exposed subglacial volcanic edifices (tuyas) in Iceland (Moore and Calk, 1991) and elsewhere (e.g., British Columbia; Dixon et al., 2002; Edwards et al., 2009; Hungerford et al., 2014), which exhibit decreasing S_{MG} with increasing elevation. Glassy hyaloclastite samples erupted at water depths >400 m (equivalent to 4 MPa hydrostatic pressure) contain $S_{MG} \geq 500$ ppm, whilst the glassy margins of all subaerial lava flow units capping tuyas are degassed to $S_{MG} \leq 200$ ppm (Moore and Calk, 1991). Similarly, glassy pillow basalt rims erupted under variable water depths off the Reykjanes Ridge (SE Iceland) indicate that sulfur is largely retained in the melt until ~200 m water depth (~2 MPa hydrostatic pressure) after which sulfur degassing takes place rapidly (Moore and Schilling, 1973). The elevated S_{MG} values observed in hydromagmatic tephra are therefore consistent with higher quench pressures, whereby rapid cooling of magma during MWI arrests degassing and thus preserves the residual melt volatile concentration at the depth of interaction (Þórðarson et al., 1996; Mastin et al., 2004).

Hawaiian basalts exhibit a similar dichotomy in volatile content between magmatic and hydromagmatic tephras, but with the transition displaced to slightly lower S contents than the more iron-rich Icelandic basalts (Moore et al., 1965; Moore and Fabbi 1971; Mastin et al., 2004; Schipper et al., 2010). Tephra from the Keanakāko'i eruption of Kīlauea (where magma interacted with a surface lake; Mastin et al., 1997) have S_{MG} between 250 and 600 ppm, which are again elevated relative to those of equivalent 'dry' Kīlauean lava fountain deposits (<100–300 ppm; e.g., Swanson and Fabbi, 1973; Mastin et al., 2004; Sides et al., 2014; Moussallam et al., 2016; Helz et al., 2017). Similarly, eruptive products from the submarine (<1400 ppm S) and subaerial (100–200 ppm S) rift zones of Mauna Loa exhibit similarly contrasting volatile contents, with glassy submarine pillow rims also preserving decreasing S and Cl concentrations with reduced water depths (Davis et al., 2003).

In this study, we interrogate volatile data from magmatic and hydromagmatic pyroclasts erupted contemporaneously during the Hverfjall Fires, Iceland, to (a) reconstruct the degassing history of magma erupted under different eruptive styles, (b) determine the magma vesicularity at the time of MWI and quenching, (c) calculate the fragmentation pressure/depth of MWI, and (d) explore how changing conditions of magma ascent and fragmentation may relate to transitions in eruptive behaviour. From these data, we consider sulfur degassing in ocean island basalts (OIB) more generally, and evaluate the use of volatiles as geochemical indicators of hydromagmatic processes.

2. Geological setting

The Hverfjall Fires (~2500 ka) was a major rifting episode within the Krafla Volcanic System, located in Iceland's Northern Volcanic Zone (Fig. 1; Þórarinsson, 1979; Sæmundsson, 1991; Mattsson and Höskuldsson, 2011; Liu et al., 2017). Effusive activity occurred intermittently along a NNE-SSW aligned fissure, which extended both north and south of the central Krafla

caldera within a graben (Sæmundsson, 1991). Most activity was concentrated at the southernmost tip of the fissure, in Mývatn, where coeval 'dry' magmatic and hydromagmatic explosive activity formed part of the Jarðbaðshólar scoria cone complex and Hverfjall tuff ring (and surrounding deposits), respectively. Hydromagmatic activity at the Hverfjall vent was initiated and maintained throughout the eruption by the interaction of magma with groundwater aquifers, with the spatial distribution of magma-water interaction (MWI) determined by the pre-existing hydrological flow regime in the region (Liu et al., 2017).

The hydromagmatic deposits from Hverfjall comprise fine-grained ash fall and massive to finely-stratified base surge units, in addition to the complex proximal stratigraphy within the tuff ring edifice itself (Sæmundsson, 1991; Mattsson and Höskuldsson, 2011). In total, hydromagmatic activity generated approximately 0.15 ± 0.02 km^3 of pyroclastic material, of which 0.08 ± 0.01 km^3 comprise an extensive fine-grained unconsolidated fall deposit formed during the initial stage of the eruption (Liu et al., 2017). Later eruptive phases were dominated by base surges with runout distances of 3–5 km. Proximal surge exposures show a clear evolution from poorly-sorted matrix-supported massive lapilli-tuff basal units (e.g., $H_{8.9}$ A; Fig. 1c, Table 1) through to well-sorted clast-supported accretionary lapilli-rich intermediate and upper units intercalated with thinly-laminated fine ash (e.g., $H_{8.9}$ F), suggesting a transition from water-saturated to drier emplacement conditions. Large angular blocks and bombs of dense basaltic lavas indicate considerable disruption of the basement substrate by subsurface explosions, although lithic clasts comprise only a minor proportion of medial to distal ash fall deposits (< 10%; Liu et al., 2017). The presence of lithic material throughout stratigraphic sections indicates continuous country rock excavation (e.g., Lorenz, 1986, 2003) and/or recycling and ejection of earlier disrupted material (Graettinger et al., 2014; Valentine et al., 2015, 2017; Lefebvre et al., 2012, 2016). However, the homogeneous lithology of basement rocks and the potential for progressive upward mixing prior to ejection means that the lithic

assemblage provides little constraint on the absolute depth of disruption (e.g., Agustín-Flores et al., 2014; Valentine et al., 2017).

'Dry' magmatic activity occurred from a vent within the Jarðbaðshólar cone complex (located ~3 km north of Hverfjall along the fissure strike), during which predominantly Strombolian activity produced a coarse, scoriaceous deposit (with a more limited dispersal distance of ~1.5 km) and subsequent lava flows (Mattsson and Höskuldsson, 2011; Liu et al., 2017). Interbedded magmatic and hydromagmatic deposits indicate that the Hverfjall and Jarðbaðshólar vents were active simultaneously (Mattsson and Höskuldsson, 2011). However, clear differences in the total grain size distribution (TGSD) of erupted tephra highlight contrasting fragmentation efficiencies at the two vents. Specifically, the opening hydromagmatic fall deposit comprises 97 wt% ash-sized material (<2 mm), of which 20 wt% is fine ash (<63 μm). In contrast, ash-sized material comprises <12% of the total mass of magmatic fall deposits (Liu et al., 2017).

The four deposit types – hydromagmatic fall, hydromagmatic surges, magmatic fall and lava flows – are rarely observed together because of the limited spatial extent of the magmatic units. However, where multiple units are exposed together (e.g., Fig. 1d), stratigraphic relationships suggest that magmatic and hydromagmatic vents were active contemporaneously (Mattsson and Höskuldsson, 2011; Liu et al., 2017). Figure 1d illustrates a representative depositional sequence observed in the field. Although the deposition of hydromagmatic material (pyroclastic fall followed by base surges) appears in many sections to have begun prior to the onset of magmatic fall, the presence of coarse magmatic lapilli directly above the Hekla-3 silicic tephra in sections proximal to Jarðbaðshólar suggest that the two vents may have initiated near-synchronously. Finely-stratified surge deposits overlying magmatic fall and lava flow units, even in proximal locations, indicates that hydromagmatic explosive activity continued at the Hverfjall vent after activity ceased at Jarðbaðshólar (Liu et al., 2017).

Overlapping vesicularity and bubble number density distributions measured in rapidly quenched magmatic and hydromagmatic pyroclasts (from the Hverfjall Fires as well as mafic eruptions more generally) indicate a shared initial history of bubble nucleation and growth, with substantial vesiculation prior to MWI (Mastin et al., 2004; Murtagh and White, 2013; Liu et al., 2017). The elevated fragmentation efficiency of hydromagmatic deposits has been attributed, at least in part, to brittle disintegration of vesicular pyroclasts due to high thermal stress generated during fast cooling (Mastin et al., 2004; Liu et al., 2015, 2017; Van Otterloo et al., 2015), although rapid steam expansion resulting from coarse mixing of magma and water also contributes to fine fragmentation by molten fuel coolant interaction (Wohletz, 1986; Zimanowski et al., 1991, 1997).

3. Material and methods

Fieldwork and sampling locations are described in detail in Liu et al. (2017); the subset of samples used in this study is listed in Table 1. Unconsolidated tephra samples were dried, sieved in phi (φ) intervals, and size fractions between -1φ (2–4 mm) and 4φ (64–125 μm) mounted in polished grain mounts. Thin sections were made through two 16–32 mm lapilli (from Jarðbaðshólar) that exhibit clear quenched rims, and through consolidated surge deposit samples comprising a range of grain sizes from -2φ (4–8 mm) to fine ash (<64 μm). No large lapilli > 8 mm were found in the unconsolidated hydromagmatic tephra deposits (Liu et al., 2017).

Major element and dissolved sulfur (S) and chlorine (Cl) concentrations of matrix glass and olivine- and plagioclase-hosted melt inclusions (MI) were measured on carbon-coated polished grain mounts using the JEOL 8530F Field Emission Gun electron microprobe (FEG-EPMA) at the University of Bristol, UK. Analyses were performed under operating conditions of 20 kV accelerating voltage and 40 nA beam current, using a defocused beam (10 μm) to

minimise sodium mobility. A combination of mineral and glass standards were used for calibration. Repeat analyses of Smithsonian basaltic glass reference materials yielded average values of 1395 ± 38 [1σ] ppm S (VG2, Juan de Fuca Ridge, NMNH 111240-52) and 168 ± 35 [1σ] ppm S (VGA-99, Mahaopuhi lava lake, Hawai'i, NMNH 113498-1), and established that no instrumental drift corrections were needed. Counting times for each element were 10 s for Na, Si, Al, K and Ca, 30 s for Mg and Fe, 40 s for P, 60 s for Mn, and 120 s for S and Cl, over a total analysis time of 120 s. Detection limits were 26 ppm (S) and 16 ppm (Cl) under the chosen operating conditions. The oxidation state of sulfur in matrix glass (magmatic and hydromagmatic) was determined from the wavelength of the S kα peak, according to the method of Carroll and Rutherford (1988; see Appendix A for full details).

To back-calculate liquid lines of descent, reverse fractional crystallisation models were initiated using the average hydromagmatic glass composition and isobaric crystallisation pressures of 0.001, 2, 4, and 6 kbar. Calculations were performed at the FMQ oxygen fugacity buffer using the mineral-melt equilibrium models of Danyushevsky (2001) for olivine, plagioclase and clinopyroxene and with Kd_{Fe-Mg}^{ol-liq} modelled after Toplis (2005). Criteria for the exclusion of mineral phases from the crystallising assemblage were Fo > 92 mol% (olivine), An > 92 mol% (plagioclase), and Mg# >90 (clinopyroxene).

H_2O and CO_2 concentrations in matrix glasses were determined by Fourier Transform Infrared Spectroscopy (FTIR) at the University of Bristol, UK. FTIR spectra were measured on doubly-polished glass wafers, with between 2 and 5 spot analyses per sample (Table S2, supplementary information). The window size was kept constant at 100×100 μm^2 for all hydromagmatic wafers (except one at 75×75 μm^2). Peak heights (absorbances) at 3550 cm^{-1} [H_2O] and 1520 and 1430cm^{-1} [CO_3^{2-} doublet] were measured using a linear baseline, and converted to absolute concentrations using the Beer Lambert Law, $c = \frac{MA_\lambda}{\rho d \varepsilon}$, where M is the molecular weight of H_2O or CO_2, A is the measured absorbance at the band of interest (λ), ρ is

229 the density of the basalt glass [2.76 g cm^3], *d* is the thickness of the glass wafer, and ε is the
230 molar absorption coefficient (H_2O: 63 L mol^{-1} cm^{-1}; Dixon et al., 1995; CO_2: 375 L mol^{-1} cm^{-1}; Fine and Stolper, 1986). Sample thicknesses were measured to a precision of ~3 μm using a
232 micrometer, and ranged from 38 to 148 μm.
233
234 **4. Results**
235 Ash particles from both hydromagmatic and magmatic deposits are mostly glassy
236 sideromelane, with phenocrysts of plagioclase, clinopyroxene, and olivine, in order of
237 decreasing abundance (Fig. 2a). Phenocrysts are present either as individual crystals or, more
238 commonly, within two- or three-phase glomerocrysts, and contain rare small melt inclusions
239 (MIs). Fe-Cu-Ni sulfide globules (<1–30 μm in diameter) are often found within the interstitial
240 glass/MIs of glomerocrysts and free phenocrysts, and, less frequently, in the matrix glass (Fig.
241 2b).
242 Matrix glasses are tholeiitic basalt in composition, containing 50.6 ± 0.2 [1σ] wt% SiO_2
243 and 5.68 ± 0.13 [1σ] wt% MgO (Table S1, supplementary information). Magmatic glasses
244 (from Jarðbaðshólar) are compositionally similar to hydromagmatic glasses (from Hverfjall),
245 but are very slightly more primitive (higher MgO content) and lie along modelled reverse
246 fractional crystallisation paths from the average hydromagmatic composition (Fig. 3b-d). Melt
247 inclusions (MIs) trapped within olivine and plagioclase phenocrysts have major element
248 compositions that are near-indistinguishable from the surrounding matrix glass, indicating melt
249 isolation during a very late-stage of fractional crystallisation (Fig. 3). Close compositional
250 agreement between olivine- and plagioclase-hosted inclusions, particularly in diagnostic
251 elements such as Fe, Ca and Al, suggest negligible post-entrapment modification due to host
252 crystallisation (no corrections have been applied). Many of the phenocrysts that host MIs

(particularly olivine) have partially to fully skeletal morphologies, suggesting rapid crystal growth (Fig. 2c).

The dissolved sulfur concentration preserved in matrix glass (S_{MG}) represents the residual sulfur remaining in the melt at the time of quenching. Quenching refers to the rapid cooling of melt to below the glass transition temperature, where the diffusivity of a volatile phase (such as S) becomes sufficiently slow that the melt concentration becomes essentially static on the timescales of interest. Figure 4 shows a clear offset in the distributions of S_{MG} between hydromagmatic (Hverfjall) and magmatic (Jarðbaðshólar) deposits. S_{MG} in magmatic ash varies between 200 and 500 ppm (average: 418 ± 93 [1σ] ppm). S_{MG} is elevated within hydromagmatic ash, and spans a much larger range, from 550 to 1450 ppm (average: 883 ± 172 [1σ] ppm). MIs preserved in all mineral phases record dissolved sulfur concentrations, S_{MI} = 1400–1700 ppm (average: 1522 ± 127 [1σ] ppm) and chlorine concentrations, Cl_{MI} = 145–200 ppm (average: 165 ± 27 [1σ] ppm; Figs. 4, 5 black crosses; Table S1, supplementary information). Assuming MIs were trapped prior to the onset of low pressure S or Cl degassing, S_{MI} and Cl_{MI} represent the maximum S and Cl contents of the magma at higher pressures. The most undegassed hydromagmatic glasses have sulfur concentrations that overlap those of co-erupted phenocryst-hosted melt inclusions. Cl concentrations in both magmatic and hydromagmatic matrix glasses (Cl_{MG}) are also generally indistinguishable from those of melt inclusions (Fig. 5), although the range of Cl_{MG} in magmatic samples extends to lower values (~110 ppm), indicating partial loss.

To test the relationship between macroscopic evidence of degassing (vesicles) and preserved volatile concentrations, we classified each compositionally analysed grain into one of three classes – dense, vesicular, or bubble shard – depending on its vesicularity and morphology, following the criteria defined by Liu et al., (2017). We find no clear correlation between the measured S_{MG} and the particle vesicularity within individual samples: dense glass

fragments, vesicular particles, and bubble shards show the same range of sulfur concentrations (Fig. 4). Temporally, a stratigraphic sequence through the surge deposits (site 8.9 A–F, where A refers to the basal sample; Fig. 4) suggests a slight shift towards higher S_{MG}, concurrent with a sedimentological transition from poorly-sorted matrix-supported lapilli-tuff (A) to well-sorted clast-supported alternations of fine ash and accretionary lapilli (C–F).

Lapilli from Jarðbaðshólar cone deposits (M_{Q1}) exhibit marked cross-sectional variations in vesicle texture. Whilst clast rims typically preserve small spherical vesicles within a glassy matrix (although with noticeable heterogeneity in spatial distribution), cores are highly vesicular with large, irregularly-shaped vesicles that are often interconnected and record expansion, coalescence and deformation. The transition between the two textural regions is often abrupt. Interstitial glass within clast cores is frequently finely microcrystalline, although regions of sideromelane can still be identified. These variations in vesicularity and vesicle morphology are accompanied by a similarly abrupt decrease in S_{MG} from rim to core, coincident with the sharp textural boundary (Fig. 6; Table S1, supplementary information). Measured profiles on three clasts show that while sulfur concentrations in the outermost (quenched) clast rim lie between 375 and 500 ppm, concentrations in the centre of the same clasts along a near-linear core to rim profile are typically 200–350 ppm and exhibit more marked local heterogeneity.

H_2O concentrations in hydromagmatic matrix glasses from the basal fall deposit range from 0.40 to 0.51 wt%, with an average of 0.45 ± 0.03 [1σ] wt% (Fig. 7; Table S2, supplementary information). Scatter in the measured concentrations increases with decreasing polished sample thickness (Fig. S1, supplementary information), and the thickest glass wafers (>100 μm) yield an average H_2O concentration of 0.43 ± 0.016 [1σ] wt%. Dissolved water is present only in the form of hydroxyl (OH^-), with no detection of a molecular water peak at 1630 cm^{-1}. This result agrees with previous FTIR studies of basaltic glass showing that at low

dissolved water contents (<0.5 wt%) hydroxyl groups are the only detectable hydrogen-bearing species (Stolper et al., 1982; Dixon et al., 1988), and provides evidence that the water is magmatic in origin. CO_2 is below detection (< ~4 ppm) in most samples, but is measurable at 14–19 ppm in four of the thickest sample wafers (>100 μm). Magmatic matrix glasses contain much lower H_2O concentrations of 0.12 ± 0.48 [1σ] wt%, with CO_2 below detection in all samples (Fig. 7).

Sulfur species in matrix glasses from the Hverfjall Fires tephra are sulfide-dominated (Fig. S2; Table S3, supplementary information), with S^{6+}/S_{total} ranging from <0.11 (hydromagmatic) and 0.04 to 0.49 (magmatic). The results are independent of the dwell time used in the analytical procedure (Appendix A, supplementary information). Using the XANES calibration of Jugo et al., (2010), measured sulfur speciation ratios yield average oxygen fugacities of FMQ +0.4 ± 0.17 (1σ; hydromagmatic) and FMQ +0.6 ± 0.33 (1σ; magmatic).

5. Discussion

5.1 Reconstructing the degassing processes

Volatile concentrations in erupted tephra provide valuable insights into the pressure/depth and timing (relative to the onset of magmatic vesiculation) of magma-water interaction, particularly when interpreted in the context of clast textures. Taking the highest S_{MI} value to represent the maximum pre-degassing sulfur concentration in the melt, the range of sulfur contents retained within hydromagmatic matrix glasses indicate that the magma had lost between 17 and 70% of its initial sulfur prior to quenching. This result demonstrates that the magma was already vesiculating at the time of MWI, consistent with previous interpretations based on clast textures and morphologies in this (Liu et al., 2017) and other hydromagmatic eruptions (e.g., Capelas tuff cone, Azores [shallow marine], Mattsson, 2010; Keanakāko'i, Hawai'i [shallow sublacustrine], Mastin et al., 2004; Askja, Iceland [subglacial], Graettinger et al., 2013).

Magmatic matrix glasses record substantially lower residual volatiles (70–83% degassed) than hydromagmatic tephra of equivalent size, despite sharing near-identical initial melt volatile concentrations (from MIs; Fig. 4) and overlapping oxidation states (from S speciation; Fig. S2). This dichotomy indicates near-surface divergence in degassing processes between hydromagmatic and magmatic vents, and could be accounted for by several potential mechanisms, including (a) post-fragmentation degassing; (b) kinetic fractionation; or (c) differences in the quench pressure (depth). Distinguishing the dominant mechanism has implications for our understanding of the respective environments and mechanisms of fragmentation (Wallace and Edmonds, 2011; Wallace et al., 2015).

Fragmentation and quenching are not always contemporaneous. Volatile losses following primary fragmentation depend on the time for individual clasts to cool to below the glass transition interval, T_g, which is in turn controlled by clast size and cooling rate (Dingwell and Webb, 1989; Lloyd et al., 2013). Importantly, the analyses shown in Figures 4 and 5 are from ash-sized particles <1 mm in diameter (unless stated), for which whole-clast cooling timescales are rapid (< 0.1 s, based on simple conductive models; Porritt et al., 2012; Helo et al., 2013). Indeed, fast cooling rates of $10^{3.7}$ – $10^{5.1}$ K s^{-1} have been determined for angular submarine hyaloclastite fragments 0.5–1 mm in diameter (Helo et al., 2013). Moreover, S_{MG} is independent of particle size in the range 0.06 to 4 mm (and the quenched rims of 16–32 mm magmatic lapilli; Fig. S3, supplementary information; note that no hydromagmatic lapilli of this grain size were found for comparison), and thus does not appear to be determined by cooling-rate. The cooling timescale for the cores of larger magmatic clasts is more protracted, however. Brittle surface cracks on many coarse lapilli and bombs indicate that the interior of the clasts remained hot enough to accommodate continued degassing and bubble expansion after the clast exterior had already cooled to below T_g (Wright et al., 2007; Porritt et al., 2012). Co-variation in S_{MG} and vesicle texture in core-to-rim profiles of magmatic lapilli (16–32 mm

353 diameter) provides geochemical evidence for extensive post-fragmentation degassing of clast
354 interiors (Fig. 6). Partial Cl degassing of some magmatic matrix glasses also reflects shallow
355 post-fragmentation volatile losses, as Cl is soluble to low pressures in basaltic melts (Fig. 5).
356 Importantly, however, S_{MG} values in both rapidly-quenched lapilli rims and in ash-sized
357 particles from the Jarðbaðshólar scoria cones are still lower than in the most degassed
358 hydromagmatic matrix glasses from Hverfjall. Post-fragmentation degassing can therefore
359 account for the range of 200–500 ppm S in magmatic matrix glasses, but an alternative process
360 is required to fully explain the difference in final volatile concentrations between magmatic
361 and hydromagmatic tephra.

362 Under conditions of disequilibrium degassing, where the magma ascent rate is faster
363 than the timescale required for volatile species to diffuse into bubbles, volatile concentrations
364 in matrix glasses are determined by the relative diffusivities of each component (kinetic
365 fractionation) rather than by their respective solubilities. Sulfur has a low diffusivity relative
366 to H_2O, which diffuses very rapidly in basaltic melts (Freda et al., 2005; Zhang and Stolper,
367 1991), and would therefore be preferentially elevated relative to H_2O in melt that had
368 experienced disequilibrium degassing. Hydromagmatic matrix glasses are elevated in both S
369 and H_2O compared to magmatic tephra of equivalent size (Fig. 7), suggesting that the
370 difference in residual sulfur content cannot be explained entirely by kinetic fractionation.
371 However, without corresponding measurements of initial H_2O concentrations (e.g., from melt
372 inclusions) or quantitative determinations of volatile diffusivities at the relevant conditions,
373 disequilibrium degassing cannot be ruled out entirely and indeed may have contributed to the
374 observed variability in S_{MG}.

375 Volatile solubilities and fluid-melt partition coefficients are strongly pressure-
376 dependent (e.g., Dixon et al., 1997; Newman and Lowernstern, 2002; Moretti et al., 2003;
377 Papale et al., 2006; Witham et al., 2012; Wallace et al., 2015; Edmonds and Wallace, 2017).

Under conditions of equilibrium degassing, and assuming no post-fragmentation losses, elevated volatile concentrations at the time of quenching are consistent with a higher saturation pressure (P_{sat}). Calculated H_2O-CO_2 saturation pressures, using the VolatileCalc thermodynamic model of Newman and Lowenstern (2002), are 1.6–2.6 MPa for Hverfjall hydromagmatic glasses, with an average of 2.1 ± 0.3 [1σ] MPa, if we assume conservatively that CO_2 is present at 0 ppm when below the FTIR detection limit. To evaluate the uncertainty in saturation pressures introduced by variation in CO_2 below the FTIR detection limit, we repeat the calculations taking CO_2 to be present at either 5 or 20 ppm; these calculations yield higher average pressures of 3.2 ± 0.3 or 6.5 ± 0.3 [1σ] MPa, respectively. Thus, for a given H_2O content, saturation pressures are extremely sensitive to the CO_2 content, such that varying CO_2 between 0 and 20 ppm produces a ~4 MPa change in P_{sat}, whilst variation in H_2O over the measured range of 0.40–0.51 wt% accounts for only 1 MPa change.

Closed-system degassing paths calculated using the SolEx multi-phase C-O-H-S model with full compositional parameterisation (Fig. 8; Witham et al., 2012) indicate a similar, but slightly higher, range of saturation pressures of 2.2–7.0 MPa for Hverfjall hydromagmatic glasses (initiated using the average melt composition from Table S1, and initial volatile concentrations of 1.2 wt% CO_2, 0.6 wt% H_2O, 1500 ppm S, and 160 ppm Cl; Neave et al., 2014; Hartley et al., 2014). Oxygen fugacity was fixed at the minimum value of NNO=0.5. Calculated H_2O-CO_2 saturation pressures obtained using either model are independent of temperature over the tested range of 1000–1150˚C.

In contrast, the lower volatile contents of magmatic glasses from Jarðbaðshólar suggest the erupted melt was degassing to near 1 atm with respect to H_2O and CO_2 (Fig. 7). Continued post-fragmentation degassing of S and Cl in magmatic tephra, however, demonstrates that not all volatile components had fully equilibrated to atmospheric conditions at the time of fragmentation.

403 Differences in the relative confining pressure at the time of fragmentation and quenching could
404 produce the contrasting residual volatile abundances in magmatic and hydromagmatic glasses.
405 Note that the hydromagmatic glasses analysed for both S and H_2O are at the upper end of the
406 range of S_{MG} measured at Hverfjall (dense sideromelane grains were preferentially selected),
407 suggesting that the calculated saturation pressures are upper bounds. The total range of S_{MG}
408 concentrations (550–1450 ppm) records quenching over a large pressure interval, from <2.6
409 MPa (or <6 MPa if uncertainty in CO_2 below the detection limit is considered) to near-
410 atmospheric conditions. Calculated degassing paths indicate that H_2O does not begin to degas
411 significantly from the melt until <6 MPa (Fig. 8), thus implying that the Hverfjall magma
412 underwent a rapid burst of vesiculation in the uppermost few hundred metres of ascent.
413 Interestingly, the SolEx solubility model, initiated using the Hverfjall Fires magma
414 composition, predicts that sulfur would begin to partition into a fluid phase at ~40–50 MPa (far
415 earlier than H_2O) and have degassed 95% of its initial sulfur by 16 MPa (Fig. 8). This result is
416 in poor agreement with our measured degassing efficiencies, which suggest up to 90% of the
417 initial sulfur is retained until <6 MPa. This discrepancy between measured and modelled sulfur
418 contents could indicate that sulfur is degassing under a conditions of significant disequilibrium.
419 However, S and Cl fluid-melt partitioning in SolEx is calibrated based on more oxidised,
420 hydrous basaltic melts (ΔNNO= +1.6 – +2.1, >3 wt% H_2O; Lesne et al., 2011; Witham et al.,
421 2012) than either Hverfjall or Kīlauea (Moussallam et al., 2016; Helz et al., 2017), in which
422 sulfur will be present largely in the form of S^{6+} and H_2O will begin to exsolve at higher pressure.
423 Sulfur solubility in basaltic melts is strongly dependent on fO_2 (see Section 4.2), and further
424 experimental and petrological work is needed to calibrate thermodynamic models for sulfur
425 degassing in reduced basaltic magmas.
426
427 **5.2 Was the Hverfjall Fires magma sulfide-saturated?**

Dissolved sulfur concentrations in reduced basaltic melts [S^{2-}] are buffered by the stability of immiscible Fe-S-O (sulfide) phases (Edmonds and Mather, 2017). Sulfur solubility is also strongly coupled to the melt FeO content as S^{2-} dissolves primarily by complexing with Fe^{2+} (Mathez, 1976; Wallace and Carmichael, 1992; O'Neill and Mavrogenes, 2002; Liu et al., 2007, Moretti and Baker, 2008), such that Fe-rich magmas can dissolve greater amounts of sulfur before reaching sulfide saturation compared to Fe-poor magmas (Wallace and Carmichael, 1992). For the Hverfjall Fires matrix glass composition (14.6 ± 0.16 [1σ] wt% FeO), the theoretical sulfur content at sulfide saturation (SCSS) is ~1800 ppm (Wallace and Carmichael, 1992; Mavrogenes and O'Neill, 1999; Wallace and Edmonds, 2011), which is in good agreement with the maximum sulfur concentration measured in melt inclusions (1737 ppm). Together with the presence of metastable Fe-Cu-Ni sulfide globules in erupted tephra (Fig. 2b), the sulfur concentrations of melt inclusions and the least degassed matrix glasses suggest that the parent magma was at, or close to, sulfide saturation throughout crystallisation and magma ascent. Late-stage degassing, in contrast, drives oxidation and progressive resorption of sulfides (Patten et al., 2013; Edmonds and Mather, 2017).

5.3 Depth of magma-water interaction during the Hverfjall Fires

Combined with additional H_2O and CO_2 measurements, our sulfur dataset places quantitative constraints on the pressures recorded by melt quenching. If quenching and fragmentation are taken to be contemporaneous during MWI (e.g. Liu et al., 2015, 2017), calculated quench pressures reflect the depth of fragmentation. This pressure-to-depth conversion requires us to consider the most appropriate pressure gradient. For the case of hydrostatic pressure, saturation pressures of 1.6–2.6 MPa (VolatileCalc) translate to fragmentation depths of 158–258 m, with an average of 210 ± 30 m. However, assuming lithostatic pressure and taking the density of the overlying country rock to be ~2.76 g cm^{-3} (dense basaltic lava flows), measured saturation

453 pressures translate to shallower fragmentation depths of 57–94 m, with an average of 74 ± 11
454 m (Fig. 9). It is worth re-emphasising that P_{sat} is highly sensitive to CO_2, particularly at the low
455 pressures of interest; therefore, the upper bound of saturation pressures may extend as high as
456 ~6 MPa (20 ppm CO_2) due to uncertainty in the absolute CO_2 concentration below the FTIR
457 detection limit.

458 Interestingly, the depth distribution for lithostatic pressure is consistent with
459 experimentally-determined optimum explosion depths of ~100 m, and maximum depths for
460 subaerial tephra ejection of ~200 m (Graettinger et al., 2014; Valentine et al., 2014). Similar
461 explosion depths of 30–115 m were derived for large blocks found in ejecta within natural
462 deposits, assuming near-optimal scaled depths (0.004 $m/J^{1/3}$) and explosion energies
463 determined from the deposit volume and calculated ejection velocities (Graettinger and
464 Valentine, 2017). Notably, these depth estimates are sensitive to both assumptions made during
465 the calculation of ejection velocities and uncertainties on the mass ejected, and so the observed
466 ejecta could easily reflect deeper source locations by 10s of metres (Graettinger and Valentine,
467 2017), thus potentially improving further the correspondence with the saturation pressures
468 calculated here. However, dissolved volatile concentrations remain elevated throughout the
469 eruption stratigraphy (Fig. 4), and it is difficult to envisage how lithostatic pressure (or close
470 to) could be maintained throughout the eruption after vent opening.

471 Alternatively, an in-vent water-saturated sediment slurry, comprising variable amounts
472 of external water, lithic material and juvenile recycled tephra (Kokelaar, 1986; White, 1996,
473 Schipper and White, 2016), would have a density intermediate between pure water and country
474 rock, and the volatile saturation pressures in quenched glass would therefore correspond to
475 fragmentation depths intermediate between lithostatic and hydrostatic end-members. The
476 presence of recycled clasts within coarse ash and lapilli from Hverfjall (Fig. 2d; Liu et al.,
477 2017) supports the magma-slurry hypothesis, as does the broad range of S_{MG} measured in

478 hydromagmatic pyroclasts (Figs. 4, 10). The substantial variations in confining pressure
479 implied by the large range of S_{MG} may record temporal or spatial variations in the water-
480 sediment proportions within the slurry and the thickness of the slurry layer itself, without the
481 need to invoke fragmentation over a large depth interval. Local pressure fluctuations resulting
482 from discrete explosions (implied by the repeating sequences of lapilli-ash graded couplets in
483 proximal deposits; Liu et al., 2017; Graettinger and Valentine, 2017) may also introduce
484 transient departures from a linear depth-pressure relationship, thus contributing further to the
485 variability in S_{MG}. During periods of high magma supply, pyroclasts in the centre of the uprush
486 column may have been thermally insulated and experienced minimal MWI, consistent with
487 observations of incandescence in the eruption column during continuous uprush phases at
488 Surtsey (Þórarinsson, 1967) and Capelinhos (Cole et al., 2001). In this case, the depth of
489 quenching may be significantly shallower than that of fragmentation. Further, as a result of
490 clast recycling within the vent slurry, sampled clasts may represent time-averaged conditions
491 over an interval longer than the deposition of an individual bed. Time-averaging in this way
492 may contribute to the apparent geochemical homogeneity (Houghton and Smith, 1993;
493 Graettinger et al., 2016; Schipper and White, 2016).

494 In the context of the regional hydrology, our geochemical data are consistent with
495 interaction with a groundwater aquifer (Liu et al., 2017), with the development of an in-vent
496 slurry maintaining and modulating confining pressures after vent opening. The opening phase
497 of hydromagmatic activity generated a widespread tephra fall deposit prior to the onset of surge
498 emplacement (Mattsson and Höskuldsson, 2011). Although vertical migration of the locus of
499 MWI could have contributed to this change in eruption style (Graettinger et al., 2014, 2015;
500 Valentine et al., 2014), the range of S_{MG} remains relatively constant between hydromagmatic
501 fall and base surge deposits, suggesting that pyroclasts were quenched under a similar range of
502 pressure conditions and arguing against significant migration of the fragmentation surface.

However, we cannot exclude small-scale migration on the scale of metres to tens of metres, as this would not be resolvable with our volatile data. In-vent recycling of pyroclasts may also have contributed to the homogenisation of subtle temporal trends. Alternatively, the transition from fall- to surge- dominated deposition may record a reduction in the volumetric magma flux, and thus a change in the magma-water mixing ratio and resultant energy transfer (Mattsson and Höskuldsson, 2011) or to variations in the vent geometry (e.g., cone growth).

Interestingly, the data shown in Figure 4 suggest a subtle increase in S_{MG} during the transition from 'wet' to 'dry' surges (inferred from sedimentological properties of the deposits; Liu et al., 2017). This increase in S_{MG} through time cannot be explained by progressive degassing of a single magma batch, which would gradually deplete sulfur in the melt. Instead, this increase may reflect either elevated confining pressure (associated with the establishment of, or changing conditions within, an in-vent magma-slurry), or small-scale (10s of metres) migration of the fragmentation level, which has been shown to influence deposition processes (Grættinger et al. 2015). Explosions beneath the centre of a pre-existing crater that occur deeper than their optimal scaled depth, form narrow debris jets that mainly collapse back into the crater (Taddeucci et al. 2013; Grættinger et al. 2014, 2015). The collapse results in the lateral displacement of gas and particles, generating dilute fine-grained density currents. These dilute flows produce fine-grained stratified and cross-stratified deposits, which closely resemble the stratified tuffs resulting from 'dry' base surges in natural systems (e.g., Waters & Fisher, 1971; Chough & Sohn 1990; Valentine et al. 2015).

The major element glass compositions of the crater samples ($H_{5.11}$) are indistinguishable from the surrounding fall and surge deposits (Fig. 3), supporting a genetic link. Nevertheless, large uncertainties remain regarding timing of edifice growth relative to the emplacement of these distal deposits. Figure 4 shows that the crater samples are slightly

527 elevated in S_{MG} relative to initial fall deposits and are instead more similar to the late-stage
528 surges ($H_{8.9}$ C–F).
529
530 **5.4 Sulfur degassing in ocean island basalts**
531 Figure 10a synthesises sulfur data in matrix glasses and melt inclusions from a range of basaltic
532 volcanic systems in Iceland. The compilation includes tephra from hydromagmatic
533 environments that include subglacial (e.g., Grímsvötn, Katla; Óladóttir et al., 2008; Sigmarsson
534 et al., 2013; Liu et al., 2015), shallow seawater (e.g., Surtsey; Schipper et al., 2015), and
535 surface/subsurface groundwater interactions (e.g., Laki; Þórðarson et al., 1996).
536 Hydromagmatic matrix glasses span a broad range in sulfur content from 1500 to 600 ppm.
537 Tephra produced during purely magmatic phases, in contrast, consistently contain <600 ppm
538 residual S_{MG} (Þórðarson et al., 1996; 2003). Co-erupted lavas typically retain S_{MG} <100 ppm,
539 indicating further degassing during flow emplacement (Þórðarson et al., 1996).
540 Vapour-saturation in reduced ocean island basalts, particularly with respect to H_2O,
541 occurs late and shallow relative to hydrous arc basalts (Gerlach, 1986; Dixon et al., 1991;
542 Wallace and Edmonds, 2011; Edmonds and Wallace, 2017), the result is a burst of vesiculation
543 at depths of only a few hundred metres beneath the ground surface. Significant sulfur loss
544 through fluid-melt partitioning into a vapour phase is therefore delayed until melts become
545 water-saturated. Figure 11 shows how vesicularity (considering here only H_2O exsolution)
546 varies as a function of pressure for mafic melts at 1125˚C, for different initial water
547 concentrations. For an initial H_2O concentration of 0.5 wt% (close to the assumed initial
548 Hverfjall concentration of 0.6 wt%), the vesicularity range of 0% (dense fragments) to ~75%
549 (highly vesicular grains) measured in hydromagmatic pyroclasts (Liu et al., 2017; blue shaded
550 region on Fig. 11) can be accounted for by quenching over a pressure range of ~1.5–4 MPa.

551 This pressure interval agrees well with the range of independent volatile saturation pressures
552 (matrix glass) determined here for the same deposit (grey shaded region on Fig. 11).

553 Bubble nucleation and growth would not only reduce the material strength of the
554 magma, thereby enabling brittle fragmentation at lower applied stresses (Wagh et al., 1993;
555 Van Otterloo et al. 2015), but may also determine the grain size distribution of fragmented
556 pyroclasts (Liu et al., 2015, 2017). Furthermore, if rapid late-stage volatile exsolution was
557 sufficient to drive magmatic fragmentation, either prior to or synchronous with MWI, then the
558 resulting increase in magma surface area would likely have enhanced the efficiency of magma-
559 water mixing and heat exchange. An interesting consideration is whether vesiculation is a
560 necessary criterion for efficient mixing between magma and water, and therefore for sustained
561 energetic MWI (Houghton et al., 2015).

562

563 **5. Summary and conclusions**

564 Dissolved volatile concentrations in magmatic and hydromagmatic tephra erupted
565 contemporaneously during the Hverfjall Fires provide important constraints on the depth and
566 timing (relative to the onset of magmatic vesiculation) of magma-water interaction (MWI). The
567 magma erupted at both Hverfjall and Jarðbaðshólar vents shared the same magmatic history
568 during dike propagation and decompression to ~1.6–2.6 MPa (average = 2.1 ± 0.3 MPa, which
569 translates to 74 m or 210 m depth assuming lithostatic or hydrostatic pressure, respectively), at
570 which point the Hverfjall magma was quenched by interaction with a system of groundwater
571 aquifers. In contrast, the Jarðbaðshólar magma continued to degas until fragmenting at near-
572 atmospheric pressure followed by late-stage expansion above the vent. This range of
573 pressures/depths for MWI agrees well with those determined from scaled analogue
574 experiments, which suggest that, for a realistic range of energies, only subsurface explosions
575 <200 m depth are likely to breach the surface while those occurring <100 m contribute most to

576 proximal−medial tephra ring deposits (Taddeucci et al. 2013; Grættinger et al. 2014, 2015;
577 Valentine et al. 2014). That these two independent approaches are converging towards a similar
578 estimate, at least within the bounds of uncertainty, is a very promising result.

579 Vesicle textures in rapidly quenched hydromagmatic tephra indicate that the magma
580 had already begun to vesiculate prior to magma-water interaction (i.e. >2–6 MPa), where
581 degassing models suggest the vapour phase would have been mostly CO_2. Sulfur remained
582 dissolved in the melt (or in sulfide phases) until shallow pressures (~2 MPa) concomitant with
583 late-stage H_2O saturation (and the onset of magmatic fragmentation?). Hydromagmatic matrix
584 glasses record elevated sulfur contents (550–1450 ppm) that reflect degassing of 17–70% of
585 the initial pre-eruptive sulfur in the melt. We attribute this heterogeneity in S_{MG} to spatial
586 variations in syn-eruptive magma-water mixing efficiency (manifest as differences in quench
587 rate) and/or to local variations in the effective confining pressure. Such a scenario is consistent
588 with existing models of magma-groundwater interaction in which MWI occurs within an in-
589 vent fluidised slurry comprising a water-saturated mixture of juvenile/recycled pyroclastic and
590 lithic debris (e.g. Hopi Buttes maar-diatreme, US; White, 1991; Surtsey tuff cone, Iceland;
591 Kokelaar, 1983, 1986; White, 1996; Schipper and White, 2016). Slurry formation provides a
592 mechanism through which the elevated confining pressures required by the volatile data could
593 be maintained and buffered throughout the eruption, whilst enabling vertical mixing and
594 ejection of fragmented juvenile and lithic material from a range of depths consistent with
595 emerging models based on experimental and natural explosion data (Graettinger et al., 2014,
596 2015; Valentine et al., 2014, Graettinger and Valentine, 2017). Furthermore, local variations
597 in confining pressure implied by the large ranges of S_{MG} might be easily envisioned within a
598 slurry environment as a result of changes in density (water-sediment proportions), slurry
599 thickness, or pore pressure. Pressure fluctuations from explosions may also contribute to
600 variable confining pressure. From a mixing perspective, the higher viscosity of a slurry relative

601 to water may enhance the efficiency of magma-water interaction, as the reduced viscosity
602 contrast with the magma would facilitate mingling.

603 Although elevated throughout, the range of sulfur concentrations in hydromagmatic
604 matrix glass remains relatively constant throughout the eruptive stratigraphy regardless of the
605 eruptive style (i.e. fall- versus surge-dominated deposition). If volatile saturation pressure is
606 taken as a proxy for fragmentation depth, these data imply that the water supply was sufficient
607 to maintain MWI throughout the eruption with no significant vertical migration in the depth of
608 interaction with time (although small-scale migration on the order of metres or tens of metres
609 cannot be excluded). Together with existing constraints on the previous extent of proto-Lake
610 Mývatn (Einarsson, 1982), this stability provides further evidence for magma-groundwater
611 interaction, rather than an eruption through a surface lake where water availability would have
612 been finite (Liu et al., 2017). However, we note that pyroclast recycling within a vent slurry
613 may have contributed to the homogenisation of temporal variability.

614 To conclude, our results support previous studies (e.g., Davis et al., 2003; Mastin et al.,
615 2004; Schipper et al., 2010a,b; 2011; Hungerford et al., 2014) that show measurements of
616 dissolved volatiles in matrix glass and melt inclusions provide an effective approach to
617 determine (1) the environment of MWI (e.g., groundwater versus surface water, vertical
618 migration of the fragmentation level) and (2) the state of the magma at the time of
619 fragmentation, both critical variables controlling the resulting eruptive style. Together, sulfur
620 and H_2O contents are sensitive indicators of hydromagmatic processes, particularly for reduced
621 Ocean Island Basalts, as late-stage volatile saturation and degassing (S, H_2O) occurs at
622 sufficiently low pressures to overlap with typical MWI environments. Although the absolute
623 constraints on P_{sat} presented here are based on H_2O contents, S provides an effective indication
624 of relative changes that can be easily measured on larger sample sizes (by EPMA) than is
625 typically achievable for H_2O (by FTIR). In response to increasing awareness that

morphological and textural pyroclast properties traditionally considered ‘diagnostic’ of MWI are non-unique indicators of fragmentation mechanisms (White and Valentine, 2016; Liu et al., 2017), we emphasise that the dissolved volatile concentrations in matrix glass provide alternative (or additional) properties by which to distinguish magmatic from hydromagmatic eruptive deposits.

Acknowledgements

This work was completed with support for KVC from the AXA Research Fund and a Royal Society Wolfson Merit Award, a Royal Society URF to ACR, and a University of Bristol postgraduate Scholarship to EJL. Fieldwork was supported by a New Researchers Award from the Geologists’ Association to EJL. We thank S. Kearns and B. Buse for their assistance with SEM analysis.

Figure Captions

Figure 1: Sample locations and field sampling of the Hverfjall eruptive deposits; (a) Location of the Krafla Volcanic System (KVS) in the larger tectonic setting of Iceland; (b) Hverfjall tuff ring viewed from the north; (c) Detailed map of the study area, with annotated locations of sampling sites from Table 1. Redrawn from Liu et al., (2017); (d) Stratigraphic section at site $H_{6.3}$ where hydromagmatic and magmatic deposits are exposed together, also showing underlying Hekla-3 silicic ash deposit. Tape measure is 70 cm for scale; (e) Characteristic erosion patterns in hydromagmatic base surge deposits at site $H_{8.9}$, viewed from the north.

650 **Figure 2:** Textural properties of erupted pyroclasts; (a) Hydromagmatic fall deposit [3φ; $H_{6.3}$];
651 (b) Plagioclase-Clinopyroxene-Olivine glomerocryst with associated Fe-Cu-Ni sulfide
652 globules [$H_{2.3}$]. Olivine has been outlined in red for clarity; (c) Skeletal olivine morphology
653 [$H_{2.3}$]; (d) Recycled crystalline lithic (cognate and/or accessory) within juvenile sideromelane
654 clast [$H_{2.3}$].
655
656 **Figure 3:** Major element matrix glass composition expressed as weight percent anhydrous
657 oxides, for the Hverfjall Fires hydromagmatic fall (blue), hydromagmatic surge (green) and
658 magmatic fall (red) deposits. Melt inclusion compositions are represented by orange (olivine-
659 hosted) and black (plagioclase-hosted) crosses; (a) SiO_2 vs. K_2O; (b) MgO vs. FeO_T; (c) MgO
660 vs. Al_2O_3; (d) MgO vs. CaO. Data for Hverfjall are presented in Table S1, supplementary
661 information. Solid lines show reverse fractional crystallisation liquid lines of descent (LLD)
662 starting from the average hydromagmatic matrix glass compositions, modelled using Petrolog3
663 (Danyushevsky and Plechov, 2011); see main text for details. Whole rock (WR) data for Krafla
664 caldera lavas from Nicholson et al., (1991).
665
666 **Figure 4:** Compilation of dissolved sulfur concentrations in matrix glass (coloured symbols)
667 and melt inclusions (black crosses). Matrix glasses analyses are coloured according to deposit
668 type (hydromagmatic fall [blue] hydromagmatic surge [green], magmatic scoria [red]) and clast
669 morphology (dense fragment [diamond], shard [triangle], or vesicular particle [circle]). All
670 clasts analysed are >0φ (<1 mm), with the exception of 20 clasts in the sample $H_{2.3}$ (2–4 mm)
671 and two lapilli in M_{Q1} (16–32 mm). Data presented in Table S1, supplementary information.
672

673 **Figure 5:** Co-variation in dissolved sulfur and chlorine concentrations in hydromagmatic fall
674 (blue filled symbols) and magmatic (red open symbols) matrix glasses, and melt inclusions
675 (black crosses) from Figure 5. Data presented in Table S1, supplementary information.
676
677 **Figure 6:** Core-to-rim profiles of matrix glass sulfur concentrations in 16–32 mm lapilli clasts
678 [M_{Q1}], showing the transition from quenched rim to expanded core. Symbols are coloured
679 according to their position within the sample: rim (filled circles) or core (crosses). The
680 backscattered electron SEM image illustrates the locations of analysis points for 'clast 1' for
681 comparison with corresponding changes in vesicle texture. Analysis points are annotated with
682 their sulfur concentration in ppm.
683
684 **Figure 7:** Co-variation in sulfur (ppm; measured by electron microprobe) and H_2O (wt%;
685 measured by FTIR spectroscopy) concentrations in matrix glasses from magmatic (red
686 triangles; H_{Q1}) and hydromagmatic (blue circles; $H_{2.3}$) pyroclasts from the 0φ (1–2 mm) size
687 class (Table S2, supplementary information). Open symbols indicate those glasses that
688 contained measurable CO_2 above the detection limit of 4 ppm. The filled square shows the H_2O
689 concentration in equilibrium with 1 atm pressure for Kīlauean ocean island basalts (0.09 ±
690 0.003 wt%; Wallace and Anderson, 1998; Mangan et al., 1993; Cashman et al., 1994; Mastin
691 et al., 2004).
692
693 **Figure 8:** Thermodynamic modelling of C-O-H-S as a function of pressure using SolEx
694 (Witham et al., 2012). Model runs were initiated using full parameterisation of the average
695 hydromagmatic glass composition (Table S1), and initial volatile concentrations of 1.2 wt%
696 CO_2, 0.6 wt% H_2O, 1500 ppm S, and 160 ppm Cl. Temperature and oxygen fugacity were fixed
697 at 1150˚C and NNO=0.5, respectively.

Figure 9: Volatile saturation pressures of hydromagmatic glasses (from Figure 8) translated to physical depths, for either lithostatic (open symbols) or hydrostatic (filled symbols) pressure gradients. The different symbols explore the effect of variable assumed CO_2 contents (0, 5, and 20 ppm) below the FTIR detection limit on the calculated pressures/depths.

Figure 10: Sulfur degassing in Ocean Island Basalts; (a) Compilation of sulfur concentrations for matrix glass (coloured symbols) and melt inclusions (black open symbols) from Icelandic glasses as a function of TiO_2/FeO (wt%), for a range of different Icelandic basaltic systems, including Hverfjall (circles; Table S1, this study), Veidivötn (vertical crosses; Þórðarson et al., 2003), Holuhraun (6-point stars; Gauthier et al., 2016), Laki (diamonds; Þórðarson et al., 1996), Grímsvötn (horizontal crosses; Sigmarsson et al., 2013; Liu et al., 2015), Katla (squares; Þórðarson et al., 2003; Óladóttir et al., 2008), Fimmsvorðuhals (5-point stars; Þórðarson et al., 2011), and Surtsey (triangles; Schipper et al., 2015). The range of sulfur concentrations within the deposits of Icelandic tuyas are shown by the vertical arrows, for subaerial lava flows (red arrow) and subaqueous deposits >400 m water depth (blue arrow; Moore and Calk, 1991). (b) Sulfur concentration of matrix glass and melt inclusions as a function of FeO wt% for Icelandic (large symbols) and Hawaiian (small symbols; Kīlauea) glasses, for comparison. Data for Kīlauea from Mastin et al., (2004), Sides et al., (2014), and Moussallam et al., (2016). The colour scheme for symbols is the same as (a). The black line corresponds to the theoretical sulfur content at sulfide saturation (SCSS) for Fe-S-O-liquid-saturated MORB melts, illustrating the dependence of sulfur solubility on melt FeO composition (Wallace and Carmichael, 1992; Mavrogenes and O'Neill, 1999, Wallace and Edmonds, 2011).

Figure 11: Vesicularity as a function of pressure for mafic melts at 1125˚C, for different initial H_2O contents (from Pioli et al., 2008), showing the range of vesicularities in hydromagmatic pyroclasts from Hverfjall (light blue shaded region; Liu et al., 2017) and the range of saturation pressures calculated in this study from glass volatile concentrations in the same deposits (grey shaded region). Symbols represent independent empirical measurements of vesicularity as a function of pressure for other volcanic systems in Iceland where quench pressure is well-constrained. [1]Dredge samples of pillow basalt rims from varying water depths off the Reykjanes Peninsula (grey crosses; Moore and Schilling, 1973); [2]Subglacial pillow basalt rims within Icelandic tuyas emplaced beneath ice of known thicknesses (black triangles; Jones, 1969).

742 **Tables**

743

744 **Table 1:** Details of the main samples used in this study. [a] Distance from centre of Jarðbaðshólar

745 vent if 'dry' magmatic or Hverfjall vent if hydromagmatic.

Sample name		**Origin**	**Deposit Type**	**GPS Location** (minutes/ degrees/ seconds)	**Distance from the vent[a] (km)**
$H_{2.3}$		Hydromagmatic	Fall	65 35 39.6 N 16 51 38.3 W	1.5
$H_{6.3}$		Hydromagmatic	Fall	65 37 57.4 N 16 50 38.0 W	3.5
$H_{9.3}$		Hydromagmatic	Fall	65 38 36.1 N 16 52 17.6 W	4.5
$H_{7.5}$		Hydromagmatic	Fall	65 39 25.6 N 16 34 02.0 W	15
H_{crater}	E (top)	Hydromagmatic	Fall/Surge	65 36 30.3 N 16 52 44.9 W	0
	C				
	A (base)				
$H_{8.9}$	F (top)	Hydromagmatic	Surge	65 37 00.9 N 16 51 27.6 W	1.5
	E				
	D				
	C				
	B				
	A (base)				
M_{Q1}		Magmatic (dry)	Fall	65 37 55.2 N 16 50 59.4 W	0.4
$M_{6.3}$		Magmatic (dry)	Fall	65 37 57.4 N 16 50 38.0 W	0.5
M_{Q3}		Magmatic (dry)	Fall	65 38 13.8 N 16 51 11.8 W	0.2

746

747

748

749

750

751 **References**

752

753 Agustín-Flores, J., Németh, K., Cronin, S. J., Lindsay, J. M., Kereszturi, G., Brand, B. D. &
754 Smith, I. E. (2014), Phreatomagmatic eruptions through unconsolidated coastal plain
755 sequences, Maungataketake, Auckland volcanic field (New Zealand), Journal of Volcanology
756 and Geothermal Research 276, 46–63.

757 Büttner, R., Dellino, P., La Volpe, L., Lorenz, V. & Zimanowski, B. (2002), Thermohydraulic
758 explosions in phreatomagmatic eruptions as evidenced by the comparison between pyroclasts
759 and products from Molten Fuel Coolant Interaction experiments, Journal of Geophysical
760 Research - Solid Earth 107(B11), 2277.

761 Carroll, M. & Rutherford, M. J. (1988), Sulfur speciation in hydrous experimental glasses of
762 varying oxidation state – results from measured wave- length shifts of sulfur X-rays, American
763 Mineralogist 73(7), 845–9.

764 Cashman, K. & Scheu, B. (2015), Magma Fragmentation, in Sigurdsson, Haraldur and
765 Houghton, Bruce and McNutt, Steve and Rymer, Hazel and Stix, John, ed., 'Encyclopedia of
766 Volcanoes', Elsevier, pp. 459–475.

767 Cashman, K. V., Mangan, M. T. & Newman, S. (1994), Surface degassing and modifications
768 to vesicle size distributions in active basalt flows, Journal of Volcanology and Geothermal
769 Research 61(1-2), 45–68.

770 Cole, P., Guest, J., Duncan, A. & Pacheco, J.-M. (2001), Capelinhos 1957– 1958, Faial,
771 Azores: deposits formed by an emergent Surtseyan eruption, Bulletin of volcanology 63(2-3),
772 204–220.

773 Colgate, S. A. & Sigurgeirsson, T. (1973), Dynamic mixing of water and lava, Nature 244,

774 552–555.

775 Danyushevsky, L. V. (2001), The effect of small amounts of H_2O on crystallisation of mid-
776 ocean ridge and backarc basin magmas, Journal of Volcanology and Geothermal Research
777 110(3-4), 265–280.

778 Danyushevsky, L.V. and Plechov, P., (2011), Petrolog3: Integrated software for modeling
779 crystallization processes, Geochemistry, Geophysics, Geosystems, 12(7).

780 Davis, M.G., Garcia, M.O. and Wallace, P., 2003. Volatiles in glasses from Mauna Loa
781 Volcano, Hawai'i: implications for magma degassing and contamination, and growth of
782 Hawaiian volcanoes. Contributions to Mineralogy and Petrology, 144(5), 570-591.

783 Dingwell, D. B. & Webb, S. L. (1989), Structural relaxation in silicate melts and non-
784 Newtonian melt rheology in geologic processes, Physics and Chemistry of Minerals, 16(5),
785 508–516.

786 Dixon, J. E. (1997), Degassing of alkalic basalts, American Mineralogist, 82(3-4), 368–378.

787 Dixon, J. E., Clague, D. A. & Stolper, E. M. (1991), Degassing history of water, sulfur, and
788 carbon in submarine lavas from Kīlauea Volcano, Hawai'i, The Journal of Geology, 99(3),
789 371–394.

790 Dixon, J. E., Stolper, E. & Delaney, J. R. (1988), Infrared spectroscopic measurements of CO_2
791 and H_2O in Juan de Fuca Ridge basaltic glasses, Earth and Planetary Science Letters 90(1),
792 87–104.

793 Dixon, J. E., Stolper, E. M. & Holloway, J. R. (1995), An experimental study of water and
794 carbon dioxide solubilities in mid-ocean ridge basaltic liquids. Part I: calibration and solubility
795 models, Journal of Petrology 36(6), 1607–1631.

796 Dixon, J.E., Filiberto, J.R., Moore, J.G. and Hickson, C.J., 2002. Volatiles in basaltic glasses
797 from a subglacial volcano in northern British Columbia (Canada): implications for ice sheet

798 thickness and mantle volatiles. Geological Society, London, Special Publications, 202(1), 255-
799 271.

800 Edmonds, M. (2008), New geochemical insights into volcanic degassing, Philosophical
801 Transactions of the Royal Society of London A: Mathematical, Physical and Engineering
802 Sciences 366(1885), 4559–4579.

803 Edmonds, M. & Mather, T. A. (2017), Volcanic sulfides and outgassing, Elements 13(2), 105–
804 110.

805 Edmonds, M. & Wallace, P. J. (2017), Volatiles and Exsolved Vapor in Volcanic Systems,
806 Elements 13(1), 29–34.

807 Edwards, B.R., Skilling, I.P., Cameron, B., Haynes, C., Lloyd, A. and Hungerford, J.H., 2009.
808 Evolution of an englacial volcanic ridge: Pillow Ridge tindar, Mount Edziza volcanic complex,
809 NCVP, British Columbia, Canada. Journal of Volcanology and Geothermal Research, 185(4),
810 251-275.

811 Einarsson, A. (1982), The palaeolimnology of Lake Mývatn, northern Iceland: plant and
812 animal microfossils in the sediment, Freshwater Biology 12(1), 63–82.

813 Fine, G. & Stolper, E. (1986), Dissolved carbon dioxide in basaltic glasses: concentrations and
814 speciation, Earth and Planetary Science Letters 76(3), 263–278.

815 Freda, C., Baker, D. R. & Scarlato, P. (2005), Sulfur diffusion in basaltic melts, Geochimica et
816 Cosmochimica Acta 69(21), 5061–5069.

817 Gauthier, P.J., Sigmarsson, O., Gouhier, M., Haddadi, B. & Moune, S. (2016), Elevated gas
818 flux and trace metal degassing from the 2014-2015 fissure eruption at the Barðarbunga volcanic
819 system, Iceland, Journal of Geophysical Research: Solid Earth.

820 Gerlach, T. M. (1986), Exsolution of H_2O, CO_2, and S during eruptive episodes at Kīlauea
821 Volcano, Hawai'i, Journal of Geophysical Research: Solid Earth 91(B12), 12177–12185.

822 Graettinger, A.H. and Valentine, G.A., 2017. Evidence for the relative depths and energies of
823 phreatomagmatic explosions recorded in tephra rings. Bulletin of Volcanology, 79(12), p.88.

824 Grættinger, A., Valentine, G., Sonder, I., Ross, P.S. & White, J. (2015), Facies distribution of
825 ejecta in analog tephra rings from experiments with single and multiple subsurface explosions,
826 Bulletin of Volcanology 77(8), 1– 12.

827 Grættinger, A., Valentine, G., Sonder, I., Ross, P.-S., White, J. & Taddeucci, J. (2014), Maar-
828 diatreme geometry and deposits: Subsurface blast experiments with variable explosion depth,
829 Geochemistry, Geophysics, Geosystems 15(3), 740–764.

830 Graettinger, A.H., Skilling, I., McGarvie, D. and Höskuldsson, Á., 2013. Subaqueous basaltic
831 magmatic explosions trigger phreatomagmatism: a case study from Askja, Iceland. Journal of
832 Volcanology and Geothermal Research, 264, pp.17-35.

833 Hartley, M. E., Maclennan, J., Edmonds, M. & Þórðarson, T. (2014), Reconstructing the deep
834 CO_2 degassing behaviour of large basaltic fissure eruptions, Earth and Planetary Science
835 Letters 393, 120–131.

836 Helo, C., Clague, D.A., Dingwell, D.B. and Stix, J., 2013. High and highly variable cooling
837 rates during pyroclastic eruptions on Axial Seamount, Juan de Fuca Ridge. Journal of
838 Volcanology and Geothermal Research, 253, pp.54-64.

839 Helz, R., Cottrell, E., Brounce, M. N. & Kelley, K. A. (2017), Olivine- melt relationships and
840 syn-eruptive redox variations in the 1959 eruption of Kīlauea Volcano as revealed by XANES,
841 Journal of Volcanology and Geothermal Research 333, 1–14.

842 Houghton, B., White, J. & Van Eaton, A. (2015), Phreatomagmatic and Related Eruption
843 Styles, in Sigurdsson, Haraldur and Houghton, Bruce and McNutt, Steve and Rymer, Hazel
844 and Stix, John, ed., 'Encyclopedia of Volcanoes', Elsevier, 537–552.

845 Hungerford, J.D., Edwards, B.R., Skilling, I.P. and Cameron, B.I., 2014. Evolution of a
846 subglacial basaltic lava flow field: Tennena volcanic center, Mount Edziza volcanic complex,
847 British Columbia, Canada. Journal of Volcanology and Geothermal Research, 272, 39-58.

848 Johnson, E. R., Wallace, P. J., Cashman, K. V. & Granados, H. D. (2010), Degassing of
849 volatiles (H_2O, CO_2, S, Cl) during ascent, crystallization, and eruption at mafic monogenetic
850 volcanoes in central Mexico, Journal of Volcanology and Geothermal Research 197(1-4), 225–
851 238.

852 Jones, J. (1969), Pillow lavas as depth indicators, American Journal of Science 267(2), 181–
853 195.

854 Jugo, P. J., Wilke, M. & Botcharnikov, R. E. (2010), Sulfur K-edge XANES analysis of natural
855 and synthetic basaltic glasses: Implications for S speciation and S content as function of
856 oxygen fugacity, Geochimica et Cosmochimica Acta 74(20), 5926–5938.

857 Kokelaar, B. (1983), The mechanism of Surtseyan volcanism, Journal of the Geological
858 Society 140(6), 939–944.

859 Kokelaar, P. (1986), Magma-water interactions in subaqueous and emergent basaltic, Bulletin
860 of Volcanology 48(5), 275–289.

861 Lefebvre, N.S., White, J.D.L. and Kjarsgaard, B.A., (2012). Spatter-dike reveals subterranean
862 magma diversions: Consequences for small multivent basaltic eruptions. Geology, 40(5), 423-
863 426.

Lefebvre, N.S., White, J.D. and Kjarsgaard, B.A., (2016). Arrested diatreme development: Standing Rocks East, Hopi Buttes, Navajo Nation, USA. Journal of Volcanology and Geothermal Research, 310, 186-208.

Lesne, P., Kohn, S. C., Blundy, J., Witham, F., Botcharnikov, R. E. & Behrens, H. (2011), Experimental simulation of closed-system degassing in the system basalt–H2O–CO2–S–Cl, Journal of Petrology 52 (9), 1737-1762.

Liu, E.J., Cashman, K., Rust, A. & Höskuldsson, A. (2017), Contrasting mechanisms of magma fragmentation during coeval magmatic and hydromagmatic activity: the Hverfjall Fires fissure eruption, Iceland, Bulletin of Volcanology 79(10), 68.

Liu, E., Cashman, K., Rust, A. & Gislason, S. (2015), The role of bubbles in generating fine ash during hydromagmatic eruptions, Geology 43(3), 239– 242.

Liu, Y., Samaha, N.-T. & Baker, D. R. (2007), Sulfur concentration at sulfide saturation (SCSS) in magmatic silicate melts, Geochimica et Cosmochimica Acta 71(7), 1783–1799.

Lloyd, A. S., Plank, T., Ruprecht, P., Hauri, E. H. & Rose, W. (2013), Volatile loss from melt inclusions in pyroclasts of differing sizes, Contributions to Mineralogy and Petrology 165(1), 129–153.

Lorenz, V. (1975), Formation of phreatomagmatic maar-diatreme volcanoes and its relevance to kimberlite diatremes, Physics and Chemistry of the Earth 9, 17–27.

Lorenz, V. (1986), On the growth of maars and diatremes and its relevance to the formation of tuff rings, Bulletin of Volcanology 48(5), 265–274.

Lorenz, V. (2003), Maar-diatreme volcanoes, their formation, and their setting in hard-rock or soft-rock environments, Geolines 15, 72–83.

886 Mangan, M. & Cashman, K. (1996), The structure of basaltic scoria and reticulite and
887 inferences for vesiculation, foam formation, and fragmentation in lava fountains, Journal of
888 Volcanology and Geothermal Research 73(1-2), 1–18.

889 Mangan, M., Cashman, K. & Newman, S. (1993), Vesiculation of basaltic magma during
890 eruption, Geology 21(2), 157–160.

891 Mangan, M. T., Cashman, K. V. & Swanson, D. A. (2014), The dynamics of Hawaiian-style
892 eruptions: a century of study, in Poland, MP and Takahashi, TJ and Landowski, CM, ed.,
893 'Characteristics of Hawaiian volcanoes', US Geological Survey, 323–354.

894 Mastin, L. G. (1997), Evidence for water influx from a caldera lake during the explosive
895 hydromagmatic eruption of 1790, Kīlauea volcano, Hawaii, Journal of Geophysical Research:
896 Solid Earth 102(B9), 20093–20109.

897 Mastin, L.G., Christiansen, R. L., Thornber, C., Lowenstern, J. & Beeson, M. (2004), What
898 makes hydromagmatic eruptions violent? Some insights from the Keanakako'i Ash, Kīlauea
899 Volcano, Hawai'i, Journal of Volcanology and Geothermal Research 137(1), 15–31.

900 Mathez, E. (1976), Sulfur solubility and magmatic sulfides in submarine basalt glass, Journal
901 of Geophysical Research 81(23), 4269–4276.

902 Mattsson, H. B. (2010), Textural variation in juvenile pyroclasts from an emergent, Surtseyan-
903 type, volcanic eruption: The Capelas tuff cone, Sao Miguel (Azores), Journal of Volcanology
904 and Geothermal Research 189(1), 81–91.

905 Mattsson, H. B. & Höskuldsson, A. (2011), Contemporaneous phreatomagmatic and effusive
906 activity along the Hverfjall eruptive fissure, north Iceland: Eruption chronology and resulting
907 deposits, Journal of Volcanology and Geothermal Research 201(1), 241–252.

908 Mavrogenes, J. A. & O'Neill, H. S. C. (1999), The relative effects of pressure, temperature and
909 oxygen fugacity on the solubility of sulfide in mafic magmas, Geochimica et Cosmochimica
910 Acta 63(7), 1173–1180.

911 Métrich, N. & Wallace, P. J. (2008), Volatile abundances in basaltic magmas and their
912 degassing paths tracked by melt inclusions, Reviews in mineralogy and geochemistry 69(1),
913 363–402.

914 Métrich, N., Bertagnini, A., Di Muro, A. et al. (2010), Conditions of Magma Storage,
915 Degassing and Ascent at Stromboli: New Insights into the Volcano Plumbing System with
916 Inferences on the Eruptive Dynamics, Journal of Petrology.

917 Métrich, N., Sigurdsson, H., Meyer, P. S. & Devine, J. D. (1991), The 1783 Lakagigar eruption
918 in Iceland: geochemistry, CO_2 and sulfur degassing, Contributions to Mineralogy and
919 Petrology 107(4), 435–447.

920 Moore, J. G. (1965), Petrology of deep sea basalt near Hawai'i, American Journal of Science
921 263(1), 40–52.

922 Moore, J. G. & Calk, L. C. (1991), Degassing and differentiation in sub- glacial volcanoes,
923 Iceland, Journal of Volcanology and Geothermal Research 46(1-2), 157–180.

924 Moore, J. G. & Fabbi, B. P. (1971), An estimate of the juvenile sulfur content of basalt,
925 Contributions to Mineralogy and Petrology 33(2), 118–127.

926 Moretti, R. & Baker, D. R. (2008), Modeling the interplay of fO_2 and fS_2 along the FeS-silicate
927 melt equilibrium, Chemical Geology 256(3), 286– 298.

928 Moretti, R., Papale, P. & Ottonello, G. (2003), A model for the saturation of COHS fluids
929 in silicate melts, Geological Society, London, Special Publications 213(1), 81–101.

930 Neave, D. A., Maclennan, J., Edmonds, M. & Þórðarson, T. (2014), Melt mixing causes
931 negative correlation of trace element enrichment and CO_2 content prior to an Icelandic
932 eruption, Earth and Planetary Science Letters 400, 272–283.

933 Newman, S. & Lowenstern, J. B. (2002), VolatileCalc: a silicate melt−H_2O−CO_2 solution
934 model written in Visual Basic for Excel, Computers & Geosciences 28(5), 597–604.

935 Óladóttir, B. A., Sigmarsson, O., Larsen, G. & Þórðarson, T. (2008), Katla volcano, Iceland:
936 magma composition, dynamics and eruption frequency as recorded by Holocene tephra layers,
937 Bulletin of Volcanology 70(4), 475– 493.

938 O'Neill, H. S. C. & Mavrogenes, J. A. (2002), The sulfide capacity and the sulfur content at
939 sulfide saturation of silicate melts at 1400 C and 1 bar, Journal of Petrology 43(6), 1049–1087.

940 Parfitt, E. A. (1998), A study of clast size distribution, ash deposition and fragmentation in a
941 Hawaiian-style volcanic eruption, Journal of Volcanology and Geothermal Research 84(3),
942 197–208.

943 Patten, C., Barnes, S.-J., Mathez, E. A. & Jenner, F. E. (2013), Partition coefficients of
944 chalcophile elements between sulfide and silicate melts and the early crystallization history of
945 sulfide liquid: LA-ICP-MS analysis of MORB sulfide droplets, Chemical Geology 358, 170–
946 188.

947 Peckover, R., Buchanan, D. & Ashby, D. (1973), Fuel–coolant interactions in submarine
948 vulcanism, Nature 245, 307–308.

949 Pioli, L., Erlund, E., Johnson, E., Cashman, K., Wallace, P., Rosi, M. & Granados, H. D.
950 (2008), Explosive dynamics of violent Strombolian eruptions: The eruption of Paricutin
951 Volcano 1943–1952 (Mexico), Earth and Planetary Science Letters 271(1), 359–368.

952 Porritt, L.A., Russell, J. K. & Quane, S.L. (2012), Pele's tears and spheres: Examples from
953 Kīlauea Iki, Earth and Planetary Science Letters 333, 171–180.

954 Rausch, J., Grobéty, B. & Vonlanthen, P. (2015), Eifel maars: Quantitative shape
955 characterization of juvenile ash particles (Eifel Volcanic Field, Germany), Journal of
956 Volcanology and Geothermal Research 291, 86–100.

957 Sæmundsson, K. (1991), Jardfrædi Kroflukerfisins, in Gardarsson, A. and Einarsson, A., ed.,
958 'Náttúra Mývatns', 662, Hid ìslenska Náttúrufrædifélag, Reykjavík, 24–95.

959 Schipper, C. I. & White, J. D. (2016), Magma-slurry interaction in Surtseyan eruptions,
960 Geology, G37480–1.

961 Schipper, C. I., Jakobsson, S. P., White, J. D., Palin, J.M. & Bush-Marcinowski, T. (2015), The
962 Surtsey Magma Series, Scientific reports 5, 11498.

963 Schipper, C. I., White, J. D. & Houghton, B. F. (2010), Syn-and post- fragmentation textures
964 in submarine pyroclasts from Loihi Seamount, Hawai'i, Journal of Volcanology and
965 Geothermal Research 191(1), 93–106.

966 Schipper CI, White JDL, Houghton BF (2011) Textural, geochemical, and volatile evidence
967 for a Strombolian-like eruption sequence at Loihi Seamount, Hawaii. J Volcanol Geotherm Res
968 207:16-32. doi:10.1016/j.jvolgeores.2011.08.001

969 Schipper CI, White JDL, Houghton BF, Shimizu N, Stewart RB (2010a) Explosive submarine
970 eruptions driven by volatile-coupled degassing at Lō`ihi Seamount, Hawai`i. Earth Planet Sci
971 Lett 295:497-510. doi:10.1016/j.epsl.2010.04.031

972 Schipper CI, White JDL, Houghton BF, Shimizu N, Stewart RB (2010b) "Poseidic" explosive
973 eruptions at Loihi Seamount, Hawaii. Geology 38:291-294. doi:doi: 10.1130/G30351.1

974 Self, S., Blake, S., Sharma, K., Widdowson, M. & Sephton, S. (2008), Sulfur and chlorine in
975 Late Cretaceous Deccan magmas and eruptive gas release, Science 319(5870), 1654–1657.

976 Sheridan, M. F. & Wohletz, K. H. (1983), Hydrovolcanism: basic considerations and review,
977 Journal of Volcanology and Geothermal Research 17(1), 1–29.

978 Sides, I., Edmonds, M., Maclennan, J., Swanson, D. & Houghton, B. (2014), Eruption style at
979 Kīlauea Volcano in Hawai'i linked to primary melt composition, Nature Geoscience 7(6), 464.

980 Sigmarsson, O., Haddadi, B., Carn, S., Moune, S., Gudnason, J., Yang, K. & Clarisse, L.
981 (2013), The sulfur budget of the 2011 Grimsvötn eruption, Iceland, Geophysical Research
982 Letters 40(23), 6095–6100.

983 Stolper, E. (1982), Water in silicate glasses: an infrared spectroscopic study, Contributions to
984 Mineralogy and Petrology 81(1), 1–17.

985 Swanson, D.A. & Fabbi, B. P. (1973), Loss of volatiles during fountaining and flowage of
986 basaltic lava at Kīlauea volcano, Hawai'i, Journal of Research of the US Geological Survey
987 1(6), 649–658.

988 Þórarinsson, S. (1967), Surtsey: The new island in the North Atlantic, Viking Press.

989 Þórarinsson, S. (1979), The postglacial history of the Mývatn area, Oikos, 17–28.

990 Þórðarson, T. & Self, S. (2003), Atmospheric and environmental effects of the 1783–1784 Laki
991 eruption: A review and reassessment, Journal of Geophysical Research: Atmospheres 108(D1),
992 2156–2202.

993 Þórðarson, T., Hayward, C., Moune, S., Hartley, M., Sigmarsson, O., Höskuldsson, A.,
994 Guðmundsson, M. & Sigmundsson, F. (2011), The 20 March–12 April 2010 Fimmvorðuhals
995 eruption, Eyjafjallajökull volcano, Iceland: Volatile contents and magma degassing,
996 Geophys. Research Abstracts 13, EGU2011–12147.

997 Þórðarson, T., Miller, D., Larsen, G., Self, S. & Sigurdsson, H. (2001), New estimates of
998 sulfur degassing and atmospheric mass-loading by the 934 AD Eldgja eruption, Iceland,
999 Journal of Volcanology and Geothermal Research 108(1), 33–54.

1000 Þórðarson, T., Self, S., Miller, D., Larsen, G. & Vilmundardottir, E. (2003), Sulphur release
1001 from flood lava eruptions in the Veidivötn, Grimsvötn and Katla volcanic systems, Iceland,
1002 Geological Society, Lon- don, Special Publications 213(1), 103–121.

1003 Þórðarson, T., Self, S., Oskarsson, N. & Hulsebosch, T. (1996), Sulfur, chlorine, and fluorine
1004 degassing and atmospheric loading by the 1783–1784 AD Laki (Skaftar Fires) eruption in
1005 Iceland, Bulletin of Volcanology 58(2-3), 205–225.

1006 Toplis, M. (2005), The thermodynamics of iron and magnesium partitioning between olivine
1007 and liquid: criteria for assessing and predicting equilibrium in natural and experimental
1008 systems, Contributions to Mineralogy and Petrology 149(1), 22–39.

1009 Valentine, G. A., Grættinger, A. H. & Sonder, I. (2014), Explosion depths for phreatomagmatic
1010 eruptions, Geophysical Research Letters, 41(9), 3045–3051.

1011 Valentine, G. A., Sottili, G., Palladino, D. M. & Taddeucci, J. (2015), Tephra ring interpretation
1012 in light of evolving maar–diatreme concepts: Stracciacappa maar (central Italy), Journal of
1013 Volcanology and Geothermal Research 308, 19–29.

1014 Valentine, G. A., White, J. D., Ross, P.-S., Graettinger, A. H. & Sonder, I. (2017), Updates to
1015 Concepts on Phreatomagmatic Maar-Diatremes and Their Pyroclastic Deposits, Frontiers in
1016 Earth Science 5, 68.

1017 Van Otterloo, J., Cas, R. A. & Scutter, C. R. (2015), The fracture behaviour of volcanic glass
1018 and relevance to quench fragmentation during formation of hyaloclastite and
1019 phreatomagmatism, Earth-Science Reviews 151, 79– 116.

1020 Wagh, A.S., Singh, J.P. and Poeppel, R.B. (1993). Dependence of ceramic fracture properties
1021 on porosity. Journal of materials science, 28(13), 3589–3593.

1022 Wallace, P. & Carmichael, I. S. (1992), Sulfur in basaltic magmas, Geochimica et
1023 Cosmochimica Acta 56(5), 1863–1874.

1024 Wallace, P. J. (2003), From mantle to atmosphere: magma degassing, explosive eruptions, and
1025 volcanic volatile budgets, in 'Developments in volcanology', 5, Elsevier, 105–127.

1026 Wallace, P. J. & Anderson Jr, A. T. (1998), Effects of eruption and lava drainback on the H_2O
1027 contents of basaltic magmas at Kīlauea Volcano, Bulletin of Volcanology 59(5), 327–344.

1028 Wallace, P. J. & Edmonds, M. (2011), The sulfur budget in magmas: Evidence from melt
1029 inclusions, submarine glasses, and volcanic gas emissions, Reviews in Mineralogy and
1030 Geochemistry 73(1), 215–246.

1031 Wallace, P. J., Plank, T., Edmonds, M. & Hauri, E. H. (2015), Chapter 7 - Volatiles in Magmas,
1032 in H. Sigurdsson, ed., 'The Encyclopedia of Volcanoes (Second Edition)', Academic Press,
1033 Amsterdam, 163 – 183.

1034 White, J. D. (1996), Impure coolants and interaction dynamics of phreatomagmatic eruptions,
1035 Journal of Volcanology and Geothermal Re- search 74(3), 155–170.

1036 White, J. D. & Valentine, G. A. (2016), Magmatic versus phreatomagmatic fragmentation:
1037 Absence of evidence is not evidence of absence, Geosphere 12(5), 1478–1488.

1038 Witham, F., Blundy, J., Kohn, S.C., Lesne, P., Dixon, J., Churakov, S.V. & Botcharnikov, R.
1039 (2012), SolEx: A model for mixed COHSCl-volatile solubilities and exsolved gas compositions
1040 in basalt, Computers and Geosciences 45, 87–97.

1041 Wohletz, K. H. (1986), Explosive magma-water interactions: Thermodynamics, explosion

1042 mechanisms, and field studies, Bulletin of Volcanology 48(5), 245–264.

1043 Wright, H. M., Cashman, K. V., Rosi, M. & Cioni, R. (2007), Breadcrust bombs as indicators
1044 of Vulcanian eruption dynamics at Guagua Pichincha volcano, Ecuador, Bulletin of
1045 Volcanology 69(3), 281–300.

1046 Zhang, Y. & Stolper, E. M. (1991), Water diffusion in a basaltic melt, Nature 351(6324), 306.

1047 Zimanowski, B., Büttner, R., Lorenz, V. & Hafele, H.-G. (1997), Fragmentation of basaltic
1048 melt in the course of explosive volcanism, Journal of Geophysical Research: Solid Earth
1049 102(B1), 803–814.

1050 Zimanowski, B., Fröhlich, G. & Lorenz, V. (1991), Quantitative experiments on
1051 phreatomagmatic explosions, Journal of Volcanology and Geothermal Research 48(3), 341–
1052 358.

Figure 1

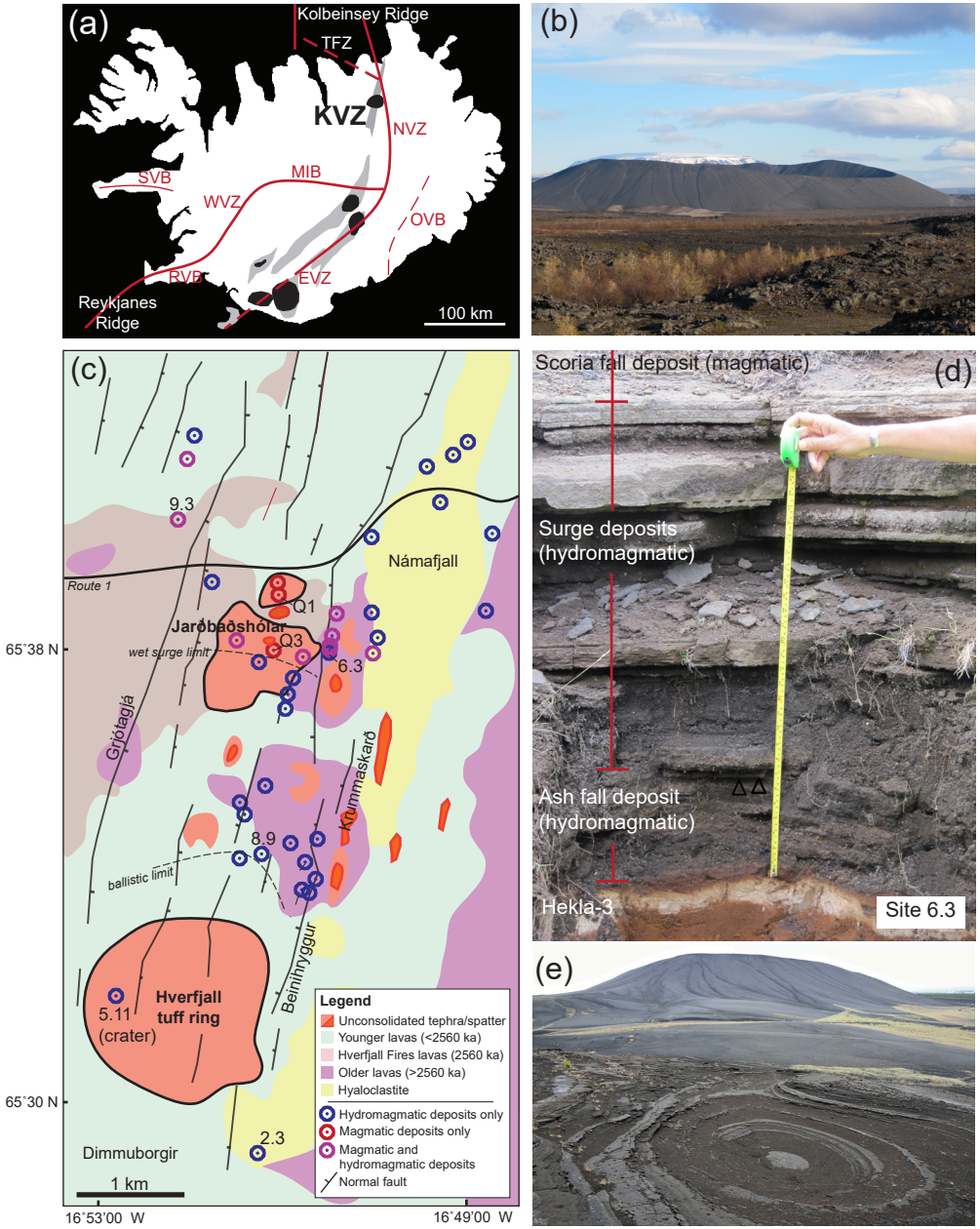
(a)
Kolbeinsey Ridge
TFZ
KVZ
NVZ
MIB
SVB
WVZ
OVB
RVB
EVZ
Reykjanes Ridge
100 km
(b)
(c)
9.3
Námafjall
Route 1
Jarðbaðshólar
Q1
Q3
wet surge limit
6.3
Grjótagjá
Krummaskarð
8.9
ballistic limit
Hverfjall tuff ring
5.11
(crater)
Beinhryggur
2.3
Dimmuborgir
1 km
65°38 N
65°30 N
16°53'00 W
16°49'00 W
Legend
Unconsolidated tephra/spatter
Younger lavas (<2560 ka)
Hverfjall Fires lavas (2560 ka)
Older lavas (>2560 ka)
Hyaloclastite
Hydromagmatic deposits only
Magmatic deposits only
Magmatic and hydromagmatic deposits
Normal fault
(d)
Scoria fall deposit (magmatic)
Surge deposits (hydromagmatic)
Ash fall deposit (hydromagmatic)
Hekla-3
Site 6.3
(e)

Figure 2

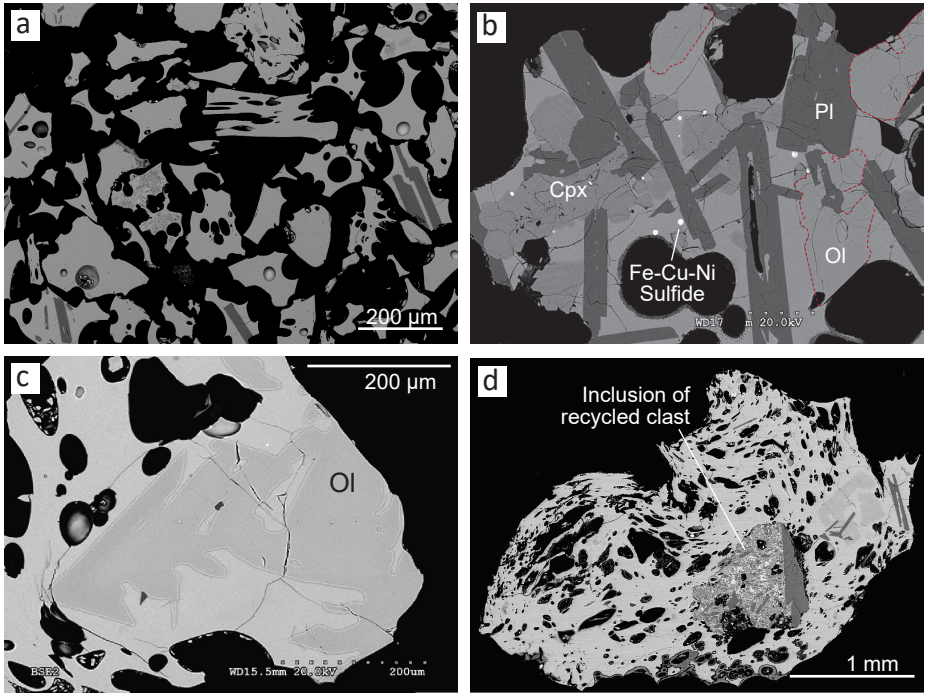
a
200 µm
b
Pl
Cpx
Ol
Fe-Cu-Ni
Sulfide
c
200 µm
Ol
d
Inclusion of
recycled clast
1 mm

Figure 3

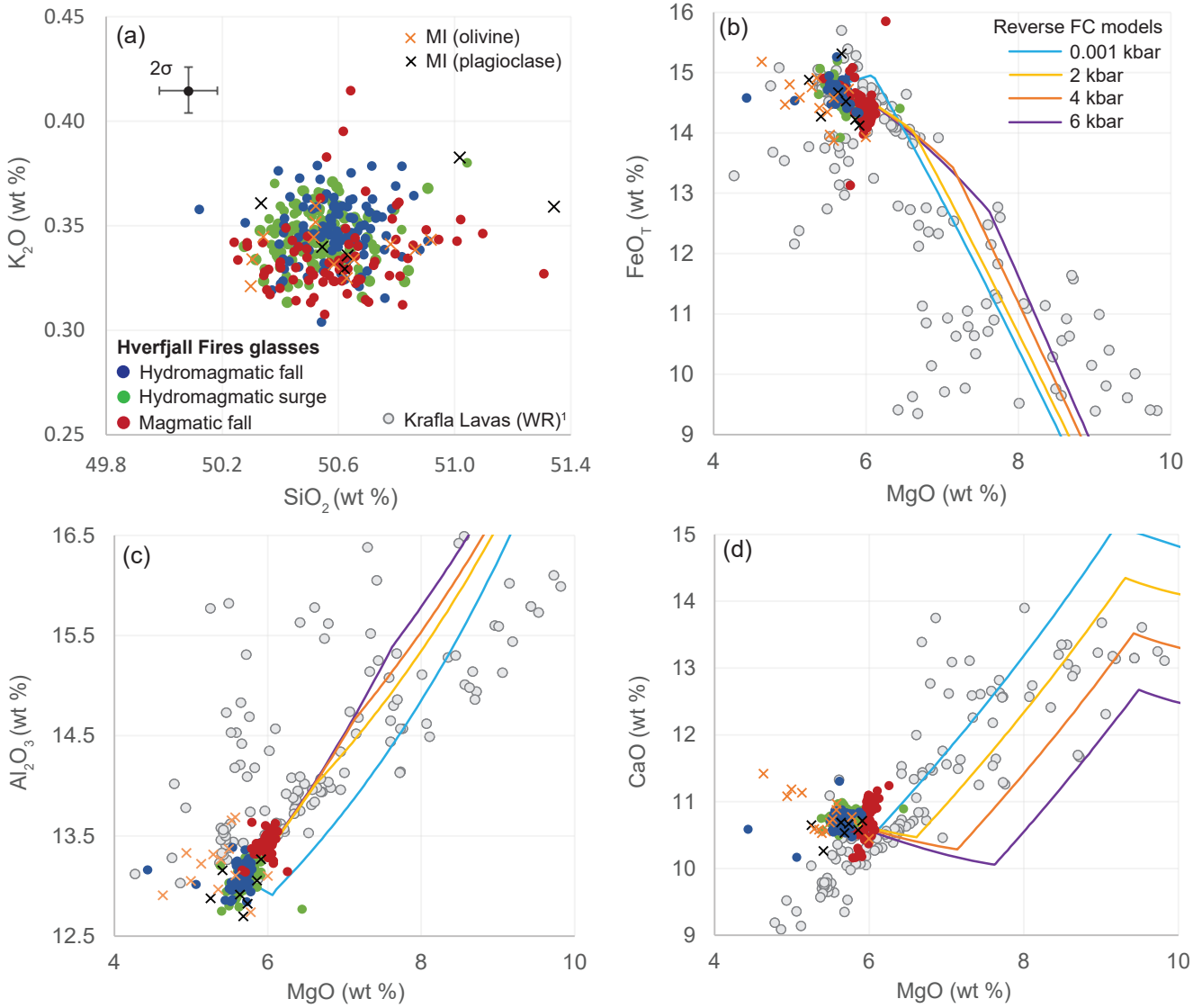
(a)
MI (olivine)
MI (plagioclase)
2σ
Hverfjall Fires glasses
Hydromagmatic fall
Hydromagmatic surge
Magmatic fall
Krafla Lavas (WR)[1]
K2O (wt %)
SiO2 (wt %)
0.45
0.40
0.35
0.30
0.25
49.8
50.2
50.6
51.0
51.4
(b)
Reverse FC models
0.001 kbar
2 kbar
4 kbar
6 kbar
FeOT (wt %)
MgO (wt %)
16
15
14
13
12
11
10
9
4
6
8
10
(c)
Al2O3 (wt %)
MgO (wt %)
16.5
15.5
14.5
13.5
12.5
(d)
CaO (wt %)
MgO (wt %)
15
14
13
12
11
10
9

Figure 4

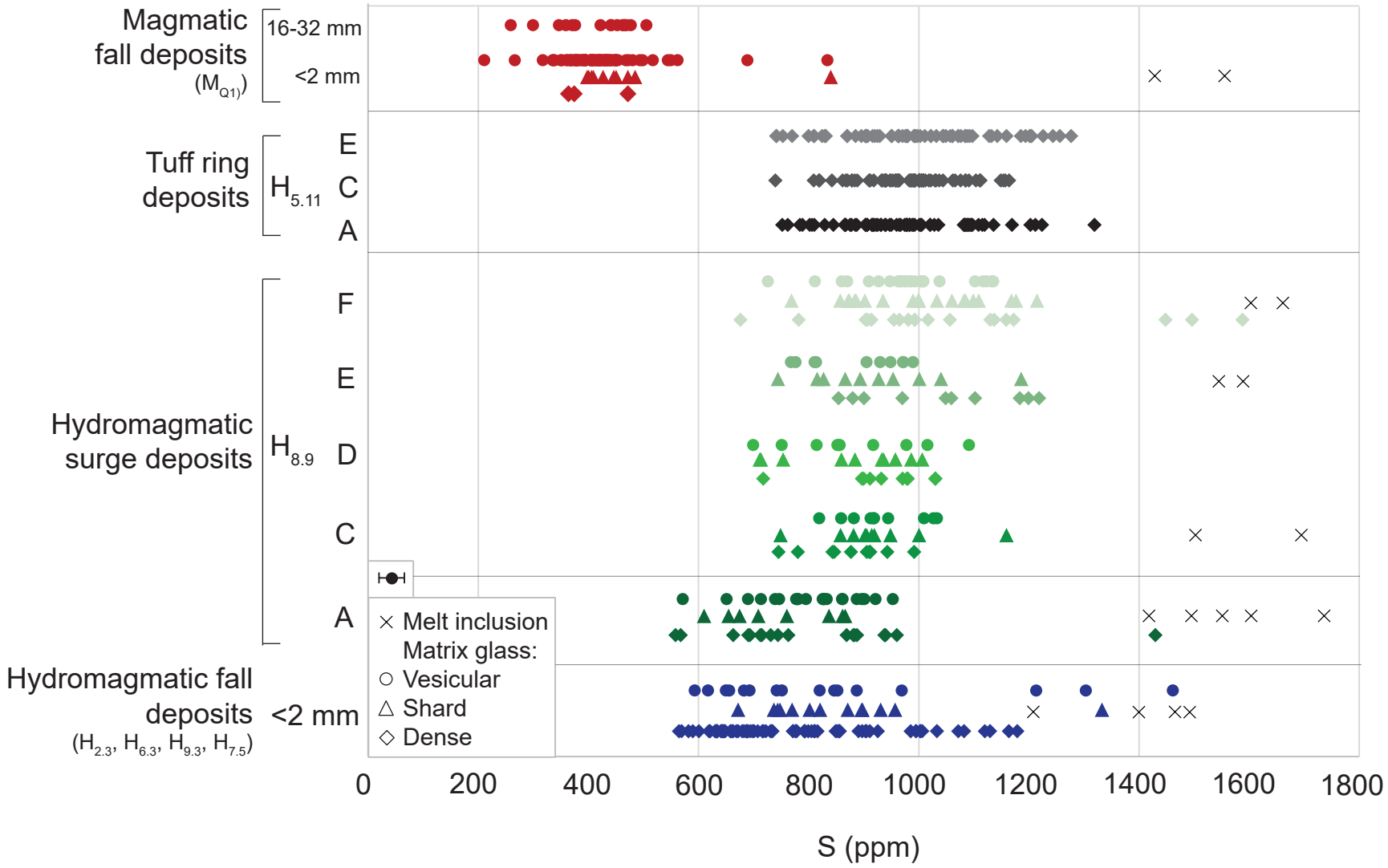
Magmatic fall deposits (M_{Q1})
16-32 mm
<2 mm
Tuff ring deposits
$H_{5.11}$
E
C
A
Hydromagmatic surge deposits
$H_{8.9}$
F
E
D
C
A
Hydromagmatic fall deposits ($H_{2.3}$, $H_{6.3}$, $H_{9.3}$, $H_{7.5}$)
<2 mm
Melt inclusion
Matrix glass:
Vesicular
Shard
Dense
0
200
400
600
800
1000
1200
1400
1600
1800
S (ppm)

Figure 5

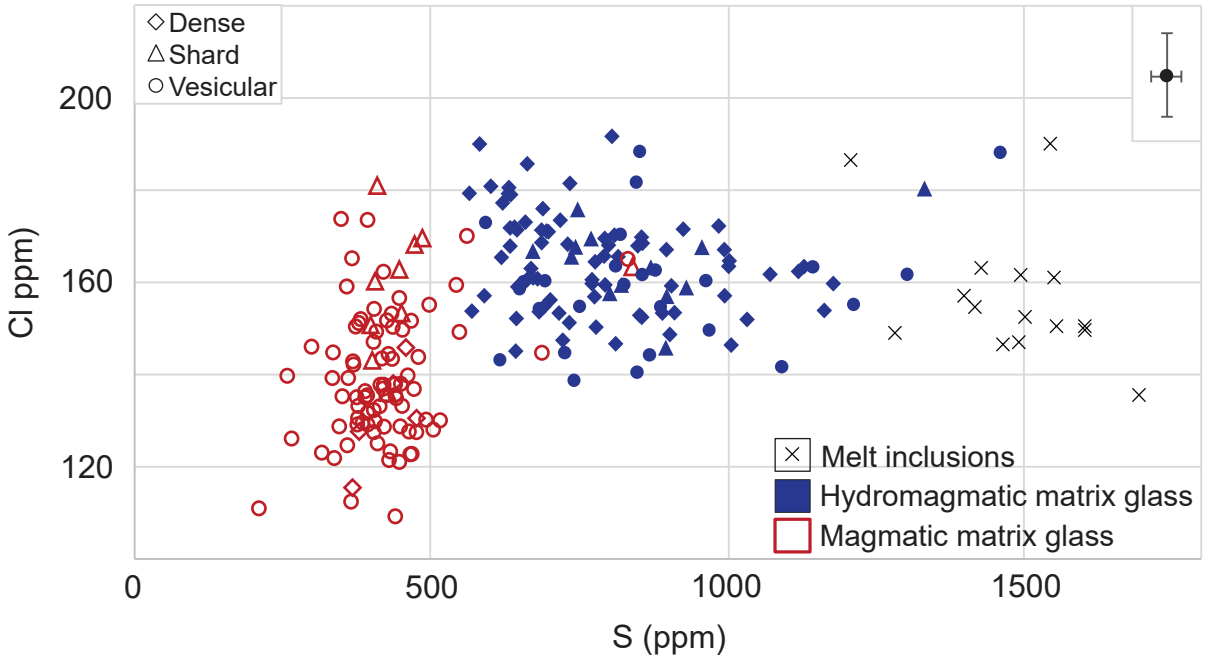
◇Dense
△Shard
○Vesicular
200
160
120
Cl ppm)
0
500
1000
1500
S (ppm)
Melt inclusions
Hydromagmatic matrix glass
Magmatic matrix glass

Figure 6

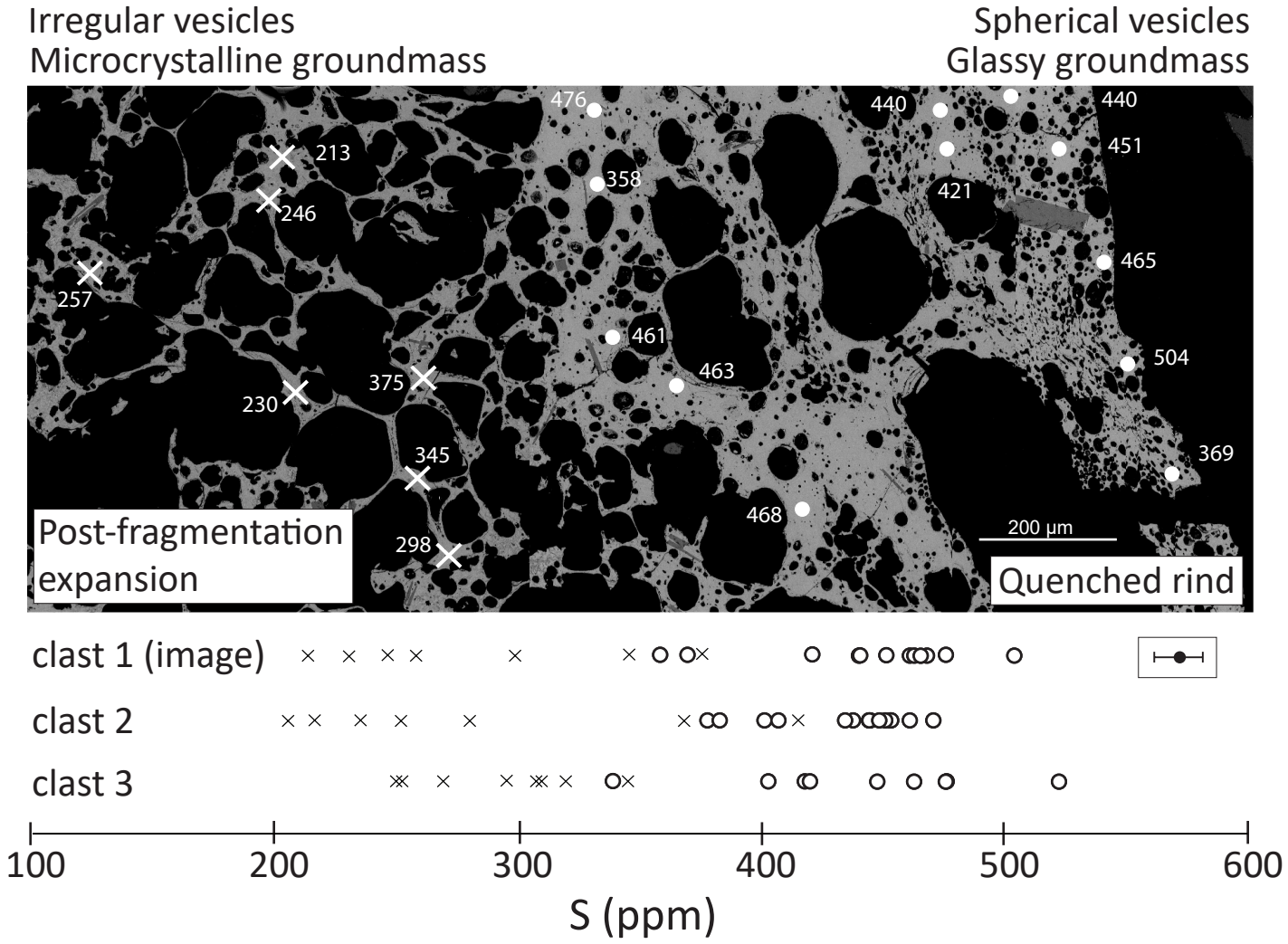
Irregular vesicles
Microcrystalline groundmass
Spherical vesicles
Glassy groundmass
476
440
440
451
213
358
421
246
465
257
461
504
463
375
230
345
369
468
200 µm
Post-fragmentation expansion
298
Quenched rind
clast 1 (image)
clast 2
clast 3
100
200
300
400
500
600
S (ppm)

Figure 7

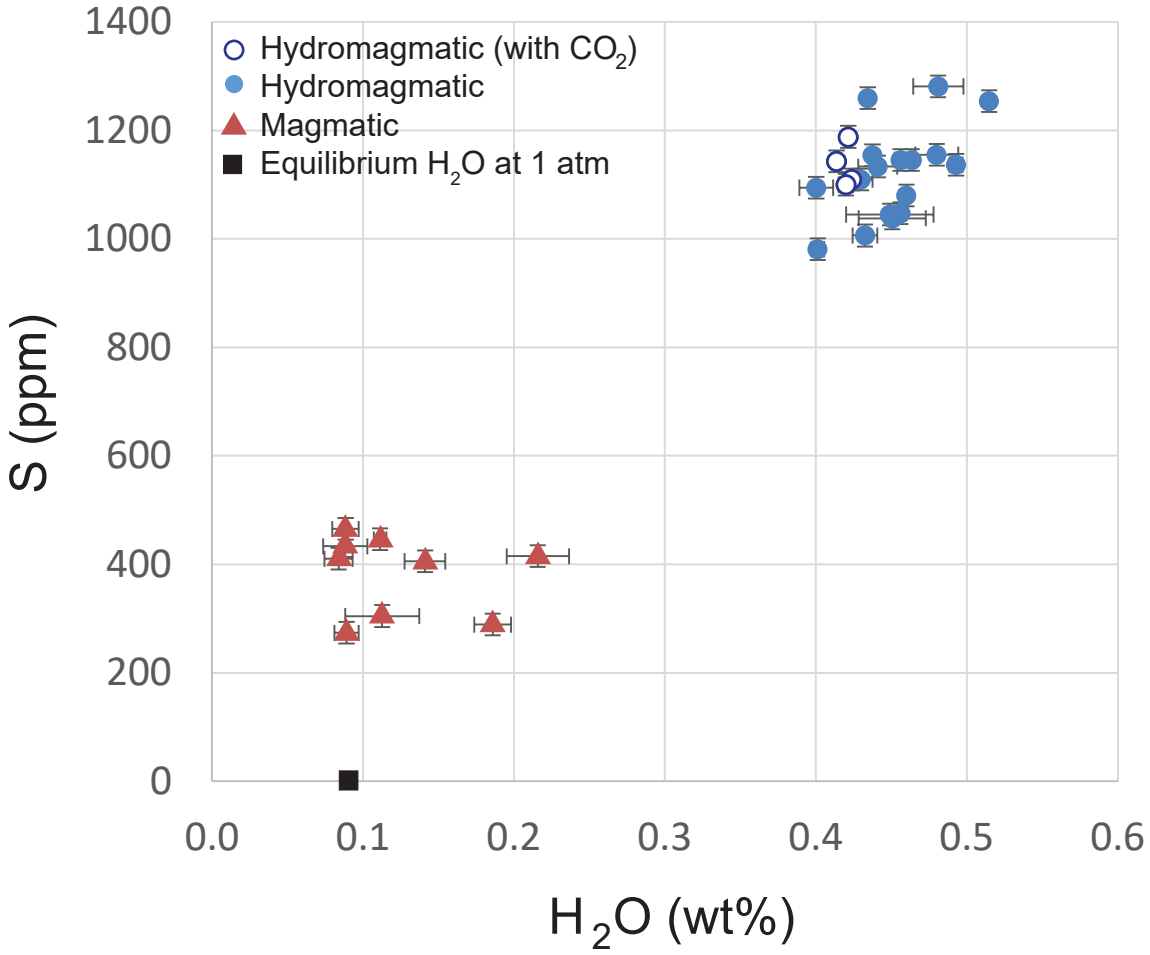
Hydromagmatic (with CO_2)
Hydromagmatic
Magmatic
Equilibrium H_2O at 1 atm
S (ppm)
1400
1200
1000
800
600
400
200
0
0.0
0.1
0.2
0.3
0.4
0.5
0.6
H_2O (wt%)

Figure 8

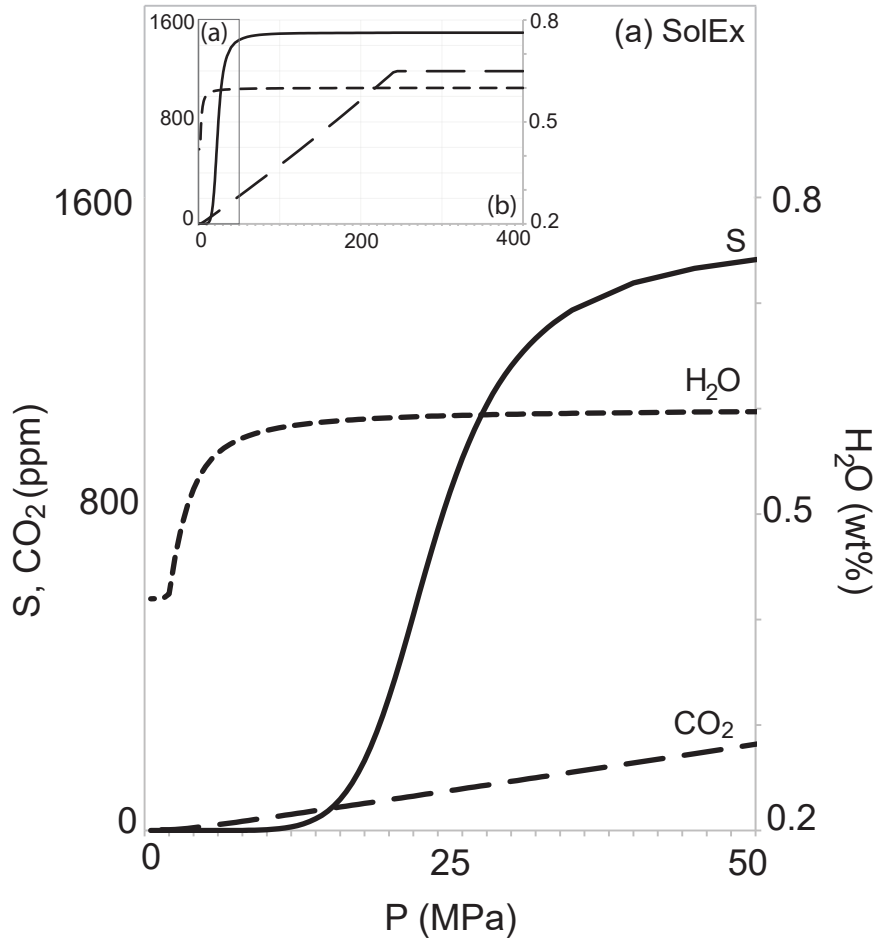
(a) SolEx
(a)
(b)
1600
800
0
0.8
0.5
0.2
200
400
S
H_2O
CO_2
S, CO_2 (ppm)
H_2O (wt%)
25
50
P (MPa)

Figure 9

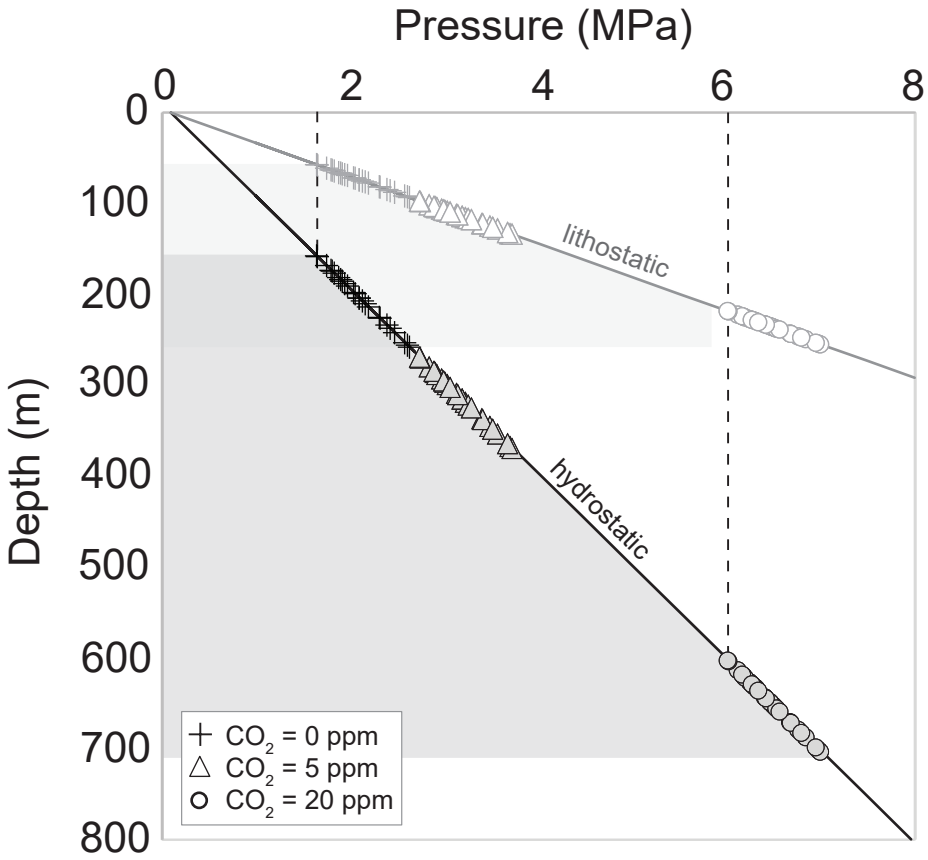
Pressure (MPa)
0
2
4
6
8
Depth (m)
0
100
200
300
400
500
600
700
800
lithostatic
hydrostatic
CO2 = 0 ppm
CO2 = 5 ppm
CO2 = 20 ppm

Figure 10

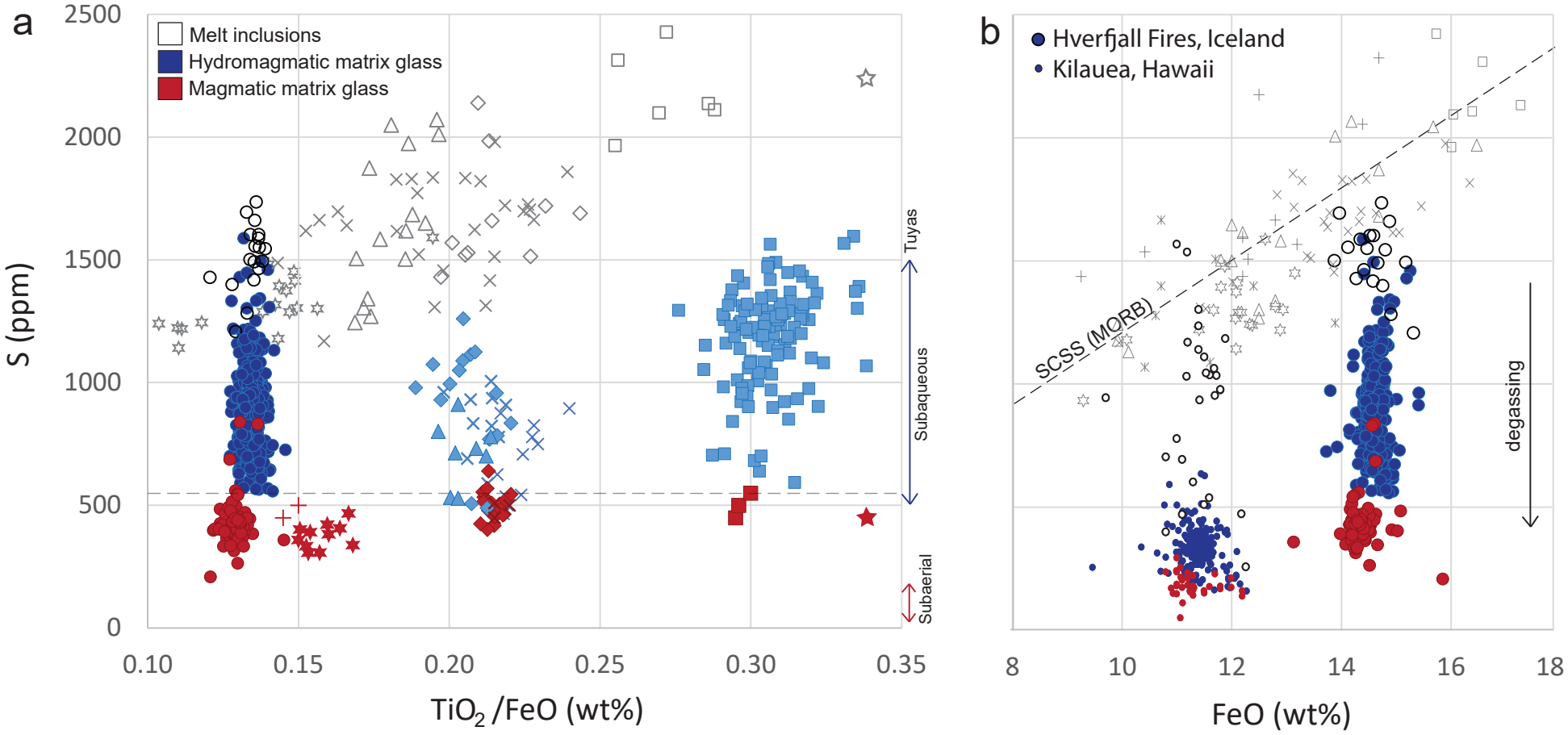
a
Melt inclusions
Hydromagmatic matrix glass
Magmatic matrix glass
S (ppm)
2500
2000
1500
1000
500
0
0.10
0.15
0.20
0.25
0.30
0.35
TiO2 /FeO (wt%)
Tuyas
Subaqueous
Subaerial
b
Hverfjall Fires, Iceland
Kilauea, Hawaii
SCSS (MORB)
degassing
8
10
12
14
16
18
FeO (wt%)

Figure 11

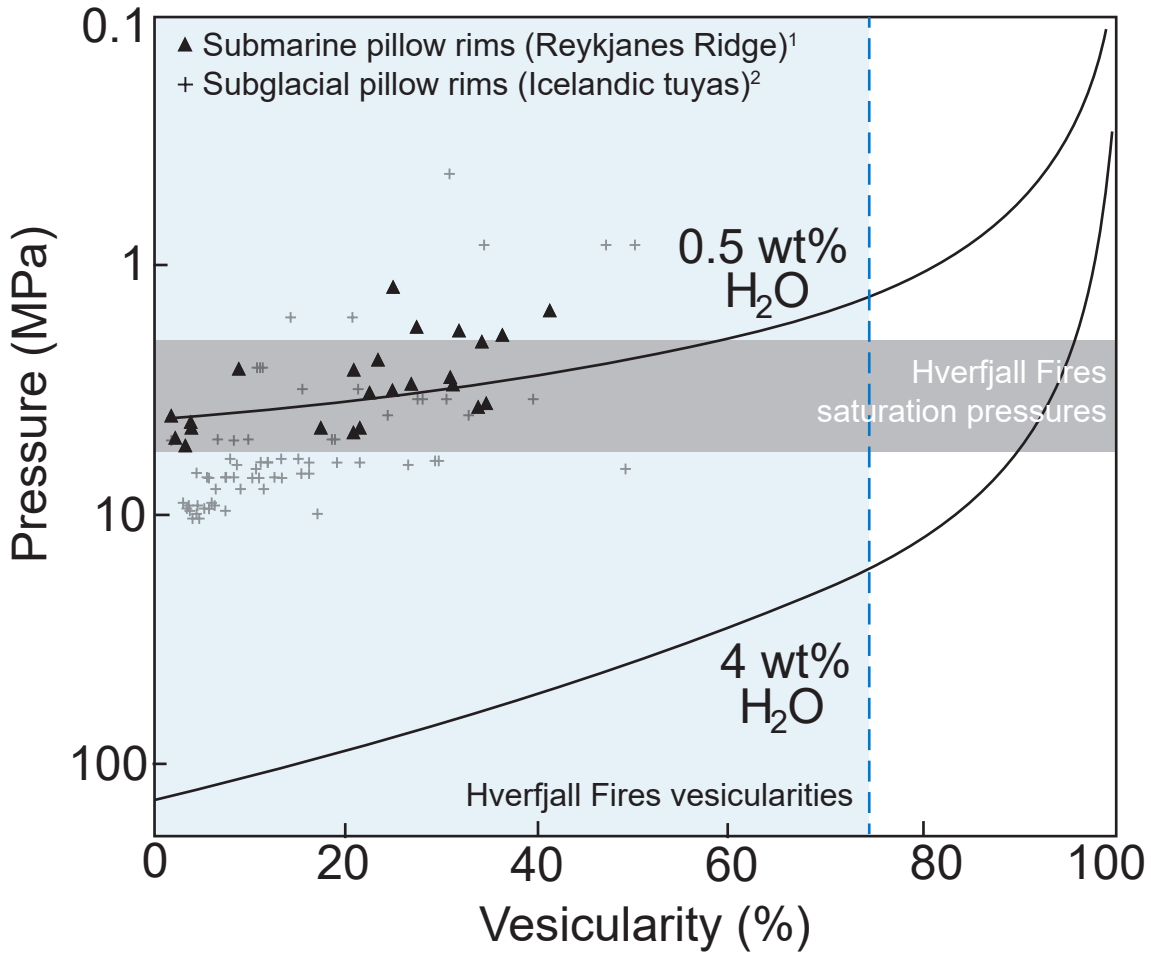
▲ Submarine pillow rims (Reykjanes Ridge)[1]
+ Subglacial pillow rims (Icelandic tuyas)[2]
0.5 wt% H2O
4 wt% H2O
Hverfjall Fires saturation pressures
Hverfjall Fires vesicularities
Pressure (MPa)
0.1
1
10
100
0
20
40
60
80
100
Vesicularity (%)

Supplementary Information to

"Insights into the dynamics of mafic magmatic-hydromagmatic eruptions from volatile degassing behaviour"

Supplementary Figures

Figure S1: Variation in dissolved water concentration in matrix glass as a function of FTIR wafer thickness. Some, but not all, hydromagmatic glasses thicker than 100 μm contain detectible (> 4 ppm) CO_2.

Figure S2: Sulfur speciation in hydromagmatic and magmatic matrix glasses, determined by the wavelength shift of the S kα peak (Wallace and Carmichael, 1994). The corresponding oxygen fugacities, expressed relative to the fayalite-magnetite-quartz (FMQ) buffer, are calculated according to the calibrations of Jugo et al., (2005; black curve) and Jugo et al., (2010; orange curve); see main text for discussion. Symbols correspond to the dwell times used during data acquisition. The Smithsonian basaltic glass standard VG2 (Juan de Fuca Ridge, NMNH 111240-52) is shown for comparison. Data presented in Table S3, supplementary information.

Figure S3: Dissolved sulfur concentration in matrix glasses as a function of particle size.

Supplementary Tables

Table S1: Major element glass compositions expressed as anhydrous oxides, with original totals, for matrix glass and melt inclusions (MI) from hydromagmatic fall, hydromagmatic surge, magmatic fall, and tuff ring crater deposits. All major elements are expressed as weight percent, with the exception of S and Cl, which are shown in ppm. Classification is based on visual observation from backscattered electron SEM images. Ol. = Olivine MI host; Plag. = Plagioclase MI host. Unconsolidated samples are analysed in individual sieved size fractions, whilst the consolidated surge deposits are analysed from thin sections comprising multiple grain sizes. Sample numbers correspond to those given in Table 1.

[see attached text file]

Table S2: H_2O-CO_2 volatile concentrations (from Fourier Transform Infrared Spectroscopy; FTIR) and corresponding major element glass compositions expressed as anhydrous oxides (from electron microprobe) for quenched matrix glasses. All major elements are expressed as weight percent, with the exception of S, Cl and CO_2, which are shown in ppm. "b.d" indicates below detection (<4 ppm for CO_2). Full results from FTIR are given in Table S1, supplementary information.

[see attached Excel file]

Table S3: Sulfur speciation in matrix glasses and corresponding melt oxygen fugacities (fO_2), expressed relative the the FMQ buffer.

[see attached Excel file]

Appendix A: Sulfur speciation and oxygen fugacity (fO_2) in quenched matrix glasses

A.1 Method

The speciation of sulfur in matrix glasses (samples $H_{2.3}$ and M_{Q1}; see main text for details) was determined from the wavelength (λ) of the S kα peak (Carroll and Rutherford, 1988; Wallace and Carmichael, 1994; Jugo et al., 2005; Lesne et al., 2011). Measurements of λ(S kα) were made using the FEG-EPMA operating under the same conditions as for major element analyses (20 kV, 40 nA), but varying the beam diameter from 10 µm (1s dwell time) to 15 µm (100 ms dwell time). For comparison, wavescans were acquired by two methods: (a) 16 static wavescans at 100 ms dwell time for each step; (b) 6 moving wavescans at 1 s dwell time for each step, migrating the beam position by 10 µm every 20 s to minimise changes in S speciation due to electron beam exposure (Wallace and Carmichael, 1994; Metrich and Clocchiatti, 1996; Wilke et al., 2008; Metrich et al., 2009).

Wavescan spectra from each method were stacked, and the S kα peak position determined by fitting a Gaussian function to the stacked spectra. The S kα peak positions of FeS_2 (pyrite) and $BaSO_4$ (barite) standards (representing pure sulfide [S^{2-}] and pure sulfate [S^{6+}] end-members, respectively) were found to be equivalent for both measurement methods, with an instrumental precision (2σ; based on 48 spectra per standard) of +/-0.006 pm (pyrite) or +/-0.015 pm (barite). The S kα peak position of VG2 basaltic glass standard was also measured.

The oxygen fugacity, fO_2, of the melt at the point of quenching to glass was calculated from S^{6+}/S_{total} according to the calibrations of Jugo et al., (2005; from EPMA) and Jugo et al., (2010; from X-ray Absorption Near Edge Structure, [XANES] spectroscopy). The assymptotic relationship between S^{6+}/S_{total} and fO_2 at low fO_2 imposes a resolution limit of ~FMQ +0, below which it is challenging to precisely constrain fO_2 by this technique.

A.2 Results

Sulfur species in matrix glasses from the Hverfjall Fires tephra are sulfide-dominated (Fig. S2; Table S3, supplementary information), with S^{6+}/S_{total} ranging from <0.11 (hydromagmatic) and 0.04 to 0.49 (magmatic). The results are independent of the analytical method used (i.e., a moving beam and 1 s dwell time [triangles; Fig. S2] or a static beam and shorter 100 ms dwell time [circles; Fig. S2]). Using the calibration of Jugo et al., (2005), average sulfur speciation values correspond to oxygen fugacities of FMQ +0.1 ± 0.36 (1σ; hydromagmatic) and FMQ +0.5 ± 0.72 (1σ; magmatic). These fO_2 ranges increase very slightly to FMQ +0.4 ± 0.17 (1σ; hydromagmatic) and FMQ +0.6 ± 0.33 (1σ; magmatic) if the calibration of Jugo et al., (2010, based on XANES spectra) is used.

A.3 References

Carroll, M. & Rutherford, M. J. (1988), Sulfur speciation in hydrous experimental glasses of varying oxidation state – results from measured wave- length shifts of sulfur X-rays, American Mineralogist 73(7), 845–9.

Lesne, P., Kohn, S. C., Blundy, J., Witham, F., Botcharnikov, R. E. & Behrens, H. (2011), Experimental simulation of closed-system degassing in the system basalt–H2O–CO2–S–Cl, Journal of Petrology 52 (9), 1737-1762.

Jugo, P. J., Luth, R. W. & Richards, J. P. (2005), Experimental data on the speciation of sulfur as a function of oxygen fugacity in basaltic melts, Geochimica et Cosmochimica Acta 69(2), 497–503.

Jugo, P. J., Wilke, M. & Botcharnikov, R. E. (2010), Sulfur K-edge XANES analysis of natural and synthetic basaltic glasses: Implications for S speciation and S content as function of oxygen fugacity, Geochimica et Cosmochimica Acta 74(20), 5926–5938.

Metrich, N. & Clocchiatti, R. (1996), Sulfur abundance and its speciation in oxidized alkaline melts, Geochimica et Cosmochimica Acta 60(21), 4151– 4160.

Metrich, N., Berry, A. J., ONeill, H. S. C. & Susini, J. (2009), The oxidation state of sulfur in synthetic and natural glasses determined by X-ray absorption spectroscopy, Geochimica et Cosmochimica Acta 73(8), 2382– 2399.

Wallace, P. J. & Carmichael, I. S. (1994), S speciation in submarine basaltic glasses as determined by measurements of SKα X-ray wavelength shifts, American Mineralogist 79, 161–167.

Wilke, M., Jugo, P. J., Klimm, K., Susini, J., Botcharnikov, R., Kohn, S. C. & Janousch, M. (2008), The origin of S^{4+} detected in silicate glasses by XANES, American Mineralogist 93(1), 235–240.

Figure S1

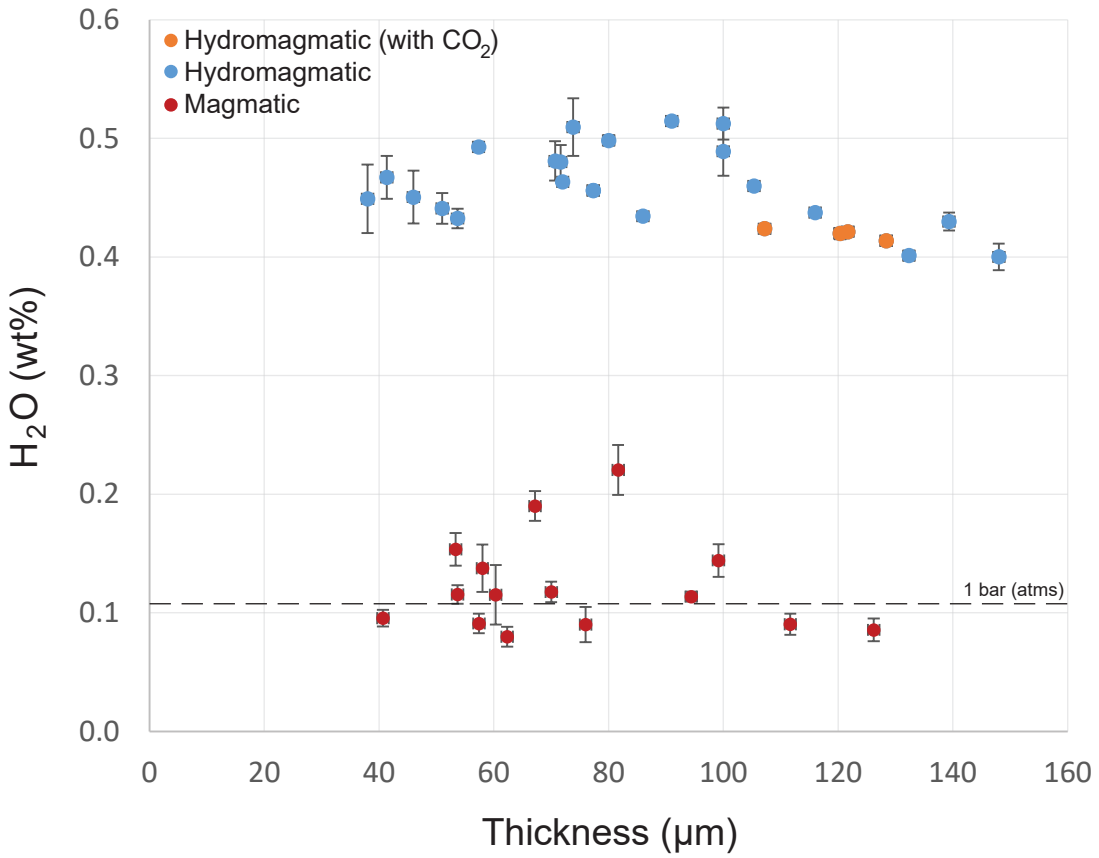
Hydromagmatic (with CO_2)
Hydromagmatic
Magmatic
1 bar (atms)
H_2O (wt%)
Thickness (μm)
0.0
0.1
0.2
0.3
0.4
0.5
0.6
0
20
40
60
80
100
120
140
160

Figure S2

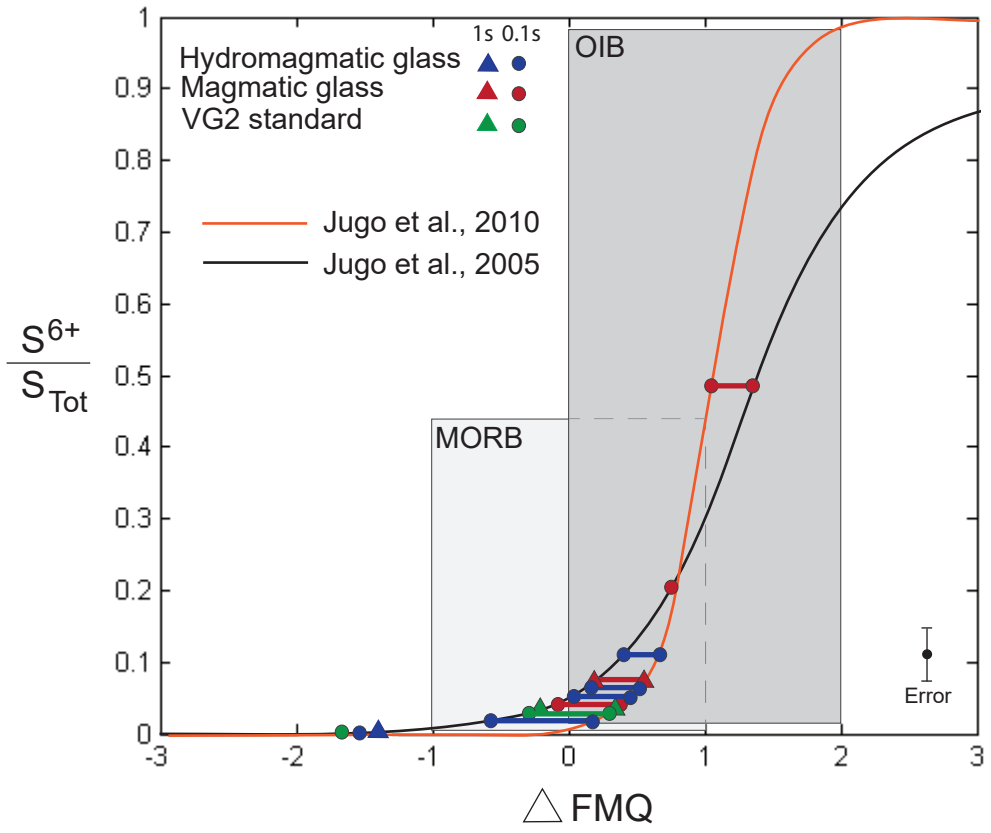
1s 0.1s
Hydromagmatic glass
Magmatic glass
VG2 standard
Jugo et al., 2010
Jugo et al., 2005
OIB
MORB
Error
$\frac{S^{6+}}{S_{Tot}}$
△FMQ
1
0.9
0.8
0.7
0.6
0.5
0.4
0.3
0.2
0.1
0
-3
-2
-1
0
1
2
3

Figure S3

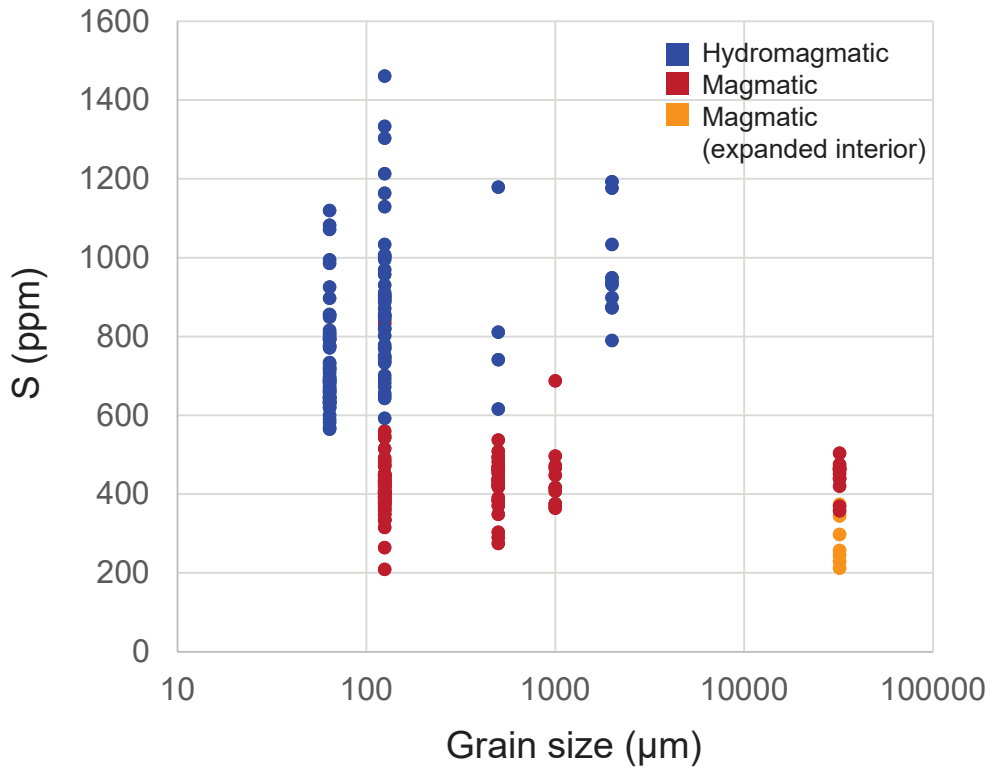
1600
1400
1200
1000
800
600
400
200
0
S (ppm)
10
100
1000
10000
100000
Grain size (μm)
Hydromagmatic
Magmatic
Magmatic
(expanded interior)